8-10-1998

Dynamics and energetics of bubble growth in magmas: Analytical formulation and numerical modeling

Alexander A. Prusevich
University of New Hampshire, Durham, alex.proussevitch@unh.edu

Dork L. Sahagian
Lehigh University

Recommended Citation
Proussevitch, A. A., & Sahagian, D. L. (1998). Dynamics and energetics of bubble growth in magmas: Analytical formulation and numerical modeling. Journal of Geophysical Research: Solid Earth, 103(B8), 18223-18251. doi:10.1029/98JB00906

JOURNAL OF GEOPHYSICAL RESEARCH, VOL. 103, NO. B8, PAGES 18,223–18,251, AUGUST 10, 1998

Dynamics and energetics of bubble growth in magmas: Analytical formulation and numerical modeling

A. A. Proussevitch and D. L. Sahagian

Institute for the Study of Earth, Oceans, and Space, University of New Hampshire, Durham

Abstract. We have developed a model of diffusive and decompressive growth of a bubble in a finite region of melt which accounts for the energetics of volatile degassing and melt deformation as well as the interactions between magmatic system parameters such as viscosity, volatile concentration, and diffusivity. On the basis of our formulation we constructed a numerical model of bubble growth in volcanic systems. We conducted a parametric study in which a saturated magma is instantaneously decompressed to one bar and the sensitivity of the system to variations in various parameters is examined. Variations of each of seven parameters over practical ranges of magmatic conditions can change bubble growth rates by 2-4 orders of magnitude. Our numerical formulation allows determination of the relative importance of each parameter controlling bubble growth for a given or evolving set of magmatic conditions. An analysis of the modeling results reveals that the commonly invoked parabolic law for bubble growth dynamics $R \sim t^{1/2}$ is not applicable to magma degassing at low pressures or high water oversaturation but that a logarithmic relationship $R \sim \log(t)$ is more appropriate during active bubble growth under certain conditions. A second aspect of our study involved a constant decompression bubble growth model in which an initially saturated magma was subjected to a constant rate of decompression. Model results for degassing of initially water-saturated rhyolitic magma with a constant decompression rate show that oversaturation at the vent depends on the initial depth of magma ascent. On the basis of decompression history, explosive eruptions of silicic magmas are expected for magmas rising from chambers deeper than 2 km for ascent rates >1-5 m s^{-1}.

1. Introduction

Bubble growth has long been recognized as a key driving mechanism of volcanic eruptions [*Sparks*, 1978; *Verhoogen*, 1951], and numerical modeling is an increasingly useful tool for understanding the processes which drive volcanic eruptions. However, whereas bubble growth has been studied in detail for various simplified systems [*Epstein and Plesset*, 1950; *Rosner and Epstein*, 1972; *Scriven*, 1959; *Szekely and Fang*, 1973], no realistic modes have been developed to date of the complex processes which drive the degassing of magmatic systems. In a previous study *Proussevitch et al.* [1993] developed a numerical model to study the growth dynamics of closely spaced bubbles under isothermal conditions. Our earlier model did not account for thermal effects of volatile vaporization or bubble expansion, or for interactions between melt properties (e.g. viscosity, diffusivity). We examined the effect of gradual decompression during diffusive bubble growth, and the detailed thermal effects of bubble growth on magmatic systems in subsequent studies [*Proussevitch and Sahagian*, 1996; *Sahagian and Proussevitch*, 1996].

The lack of the thermal effects and variations of melt properties limited the volcanic relevance of the previous model to cases of melt degassing at high pressures (>70 MPa) where the heat of water vaporization is very small [*Sahagian and Proussevitch*, 1996]. However, these pressures are not appropriate for the upper part of the volcanic conduit and vent where the most rapid degassing and bubble growth occurs in subaerial eruptions. The goal of the present study is to construct a testable numerical model for the dynamics of bubble growth which includes thermal effects and the effects of parametric interactions during decompressive and diffusive degassing. We have extended the previous model by incorporating the hydrodynamic and thermodynamic effects of bubble growth.

These newly incorporated effects include (1) Temperature and volatile concentration dependent melt viscosity and species diffusion coefficient which can vary by a few orders of magnitude across the bubble wall; (2) Work of gas expansion (pdV) during bubble growth and decompression which can cause a drop in temperature of 15-20 K for every 100 MPa of adiabatic melt decompression during equilibrium degassing; (3) Heat of exsolution, most important at low pressures [*Sahagian and Proussevitch*, 1996] (magma cooling due to heat of exsolution of 1 wt% of oversaturated water at atmospheric pressure can reach 8 K, an effect which must be accounted for in any realistic magmatic bubble growth model); (4) Latent heat of melt vitrification (or crystallization), if exsolution and pdV work cause sufficient cooling of the melt; and (5) Viscous heating due to bubble expansion.

Paper number 98JB00906.
0148-0227/98/98JB-00906$09.00

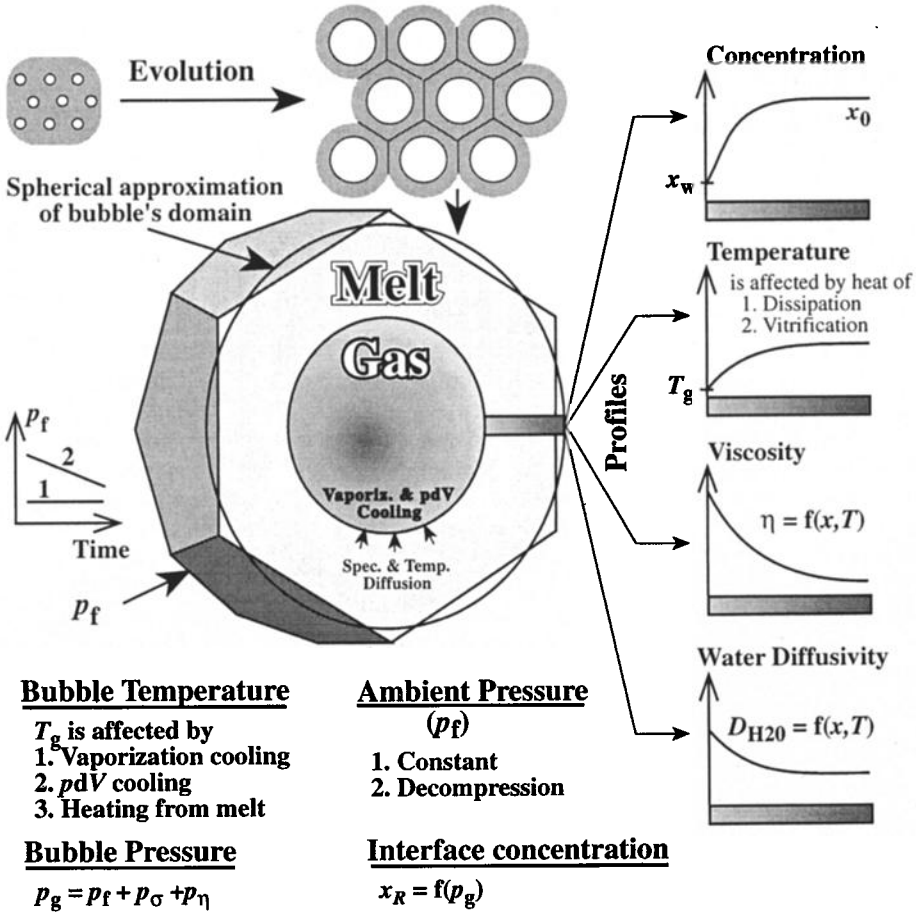

Figure 1. Geometry and conditions of the bubble growth model. Initial bubbles are in a closely packed structure which enables us to define a unit cell which includes a single bubble surrounded by a finite volume of melt. The polygonal elementary cell is approximated as spherical with a bubble at its center, thus reducing the three-dimensional computational domain to one-dimension with negligible loss of accuracy [*Princen*, 1979]. Bubble growth dynamics and evolution of a large gas-melt system is controlled by decompression, change of volatile solubility at the bubble interface, and diffusion into the bubble. Gas and melt temperatures change during degassing because of vaporization and pdV cooling, viscous dissipation, and vitrification heating as distributed by thermal diffusivity in the melt. The model accounts for interaction between parameters (e.g., viscosity, diffusivity, etc.), all of which are dependent on temperature and volatile content. The model conditions and assumptions contrast sharply with those of the simple isothermal model developed earlier [*Proussevitch et al.*, 1993].

The rheology of magmatic foam can differ significantly from that of melt with more widely separated bubbles [*Bagdassarov and Dingwell*, 1992, 1993; *Bagdassarov et al.*, 1994]. The contrast depends on bubble volume fraction and is relevant only for late stages of magma rise near the vent. At high strain rates many silicic melts exhibit nonlinear viscoelasticity [*Webb and Dingwell*, 1990]. However, relatively low strain rates are associated with bubble growth considered in the present study, so Newtonian rheology is considered appropriate.

The basic tenets of the present model are inherited, in part, from our previous isothermal model [*Proussevitch et al.*, 1993]. While the previous model was not generally applicable to real eruptions, we now attempt to reduce the broad gap between natural systems and the simple formulations involved in numerical modeling. In general, the model involves the simultaneous solution of a system of equations including mass, momentum, and energy transfer between an expanding bubble and the surrounding melt. The physical conditions of our model are as follows (Figure 1):

1. We use a spherical coordinate system with its origin at the bubble center.

2. Each bubble is surrounded by a concentric shell of melt of finite volume. The volume of the shell reflects bubble number density. While the packing of spherical rather than polyhedral elementary cells is not perfect, errors can be made negligible by including overlap to offset gaps [*Princen*, 1979; *Proussevitch et al.*, 1993].

3. Bubble growth is driven by diffusion of volatiles from the surrounding melt. Volatile concentration at the bubble interface is in equilibrium with gas pressure within the bubble. The diffusion coefficients of multiple volatile components (e.g., H_2O and CO_2) are coupled in the model,

but we will limit our discussion to water. We assume that the kinetics of the ion-gas molecular transition at the melt-bubble interface is rapid and not a rate-limiting factor for mass flux into the bubble [*Zhang et al.*, 1995].

4. Temperature within the bubble is controlled by cooling due to the heat of volatile exsolution and the work involved in bubble expansion. The latter is partially compensated by heat flux from the surrounding melt which is heated due to viscous dissipation in response to bubble growth. (If crystallization occurs, this also heats the melt.)

5. Melt viscosity and volatile diffusivity are functions of temperature and volatile concentration in the surrounding melt.

6. Ambient pressure is held constant in our discrete parametric analysis and decreases at a constant rate in our idealized eruption model.

7. Our analysis does not account for nucleation of additional (younger) bubbles. It involves a system of uniformly spaced bubbles (Figure 1) nucleated simultaneously. While this may apply to many systems [*Toramaru*, 1989, 1995], it may not hold for others in which there are high rates of bubble nucleation on preexisting nuclei (heterogenous nucleation) or in the melt (homogeneous nucleation). All bubbles in the modeled system have an equal volume of melt which provide volatiles by diffusion, and thus they all grow to the same final size. As a result, the model does not produce the bubble size distribution which would arise from a naturally expected nonuniform spacing of individual bubbles in the system. This would require a great deal of additional computational resources but could ultimately discriminate the contribution of the bubble size distribution caused by uneven initial bubble spacing from that caused by different nucleation timing.

We have developed an analytical formulation of bubble growth in magmatic systems which includes the factors described above (see appendices). The formulation is summarized in Table 1. Based on our analytical formulation we have developed a numerical model (see appendix B) which explores many previously unrecognized processes in volcanic systems. Because there are many variables involved in bubble growth, it is computationally efficient to define a set of nondimensional equations to described the system. In some previous analyses [*Rosner and Epstein*, 1972; *Szekely and Fang*, 1973], nondimensionalization was performed in order to obtain analytical solutions of simple formulations using asymptotic approximations which discount many variables but allow for analytical solution. In contrast, the purpose of nondimensionalization in our analysis is to provide a useful transformation of the original analytical equations for numerical solution in order to reduce the order of differential equations, improve convergence, reduce the number of iterations, and increase precision. This dramatically simplifies computational procedures, reduces CPU time and increases precision while not neglecting any parameters and variables.

We used our numerical model to run two sets of numerical "experiments" to explore the sensitivity of the system and to examine model performance in a few controlled (but not fully realistic) geological scenarios. In one set of experiments the model was run to conduct a parametric study in which the sensitivity of diffusive bubble growth to various magmatic parameters was explored in detail. We ran the model to examine parametric nonisothermal bubble growth with a range of parameter values appropriate for natural volcanic systems. The sensitivity of bubble growth dynamics to variations of initial values of each parameter was determined by holding all other initial values constant. This involved instantaneous decompression from various initial pressures to 1 bar (parametric study), as was done in the relatively primitive isothermal model [*Proussevitch et al.*, 1993]. However, unlike our previous study, we now include the effects of interaction between parameters, so that all parameters are time dependent.

A second set of model runs involved gradual decompression to simulate rising magma in which the effects of the decompression rate as well as the interactions of diffusion and decompression are considered (constant decompression study). The model accounts for the interaction of ambient pressure (decompression) with various melt parameters such as diffusivity, viscosity, surface tension, etc., in addition to their interactions with each other. Magma parameters were selected corresponding to generalized basaltic and rhyolitic magmas. The details of magma chemistry are not explored as the relevant parameters and relationships between magma properties were assigned values directly. While there are many magmatic compositions which will lead to other parameter values, the range included here should cover some typical magmas.

The parametric study was designed to illustrate diffusive bubble growth (pure oversaturation degassing), while the constant decompression study reflects the more geologically relevant case of a combination of oversaturation and equilibrium degassing.

1. Diffusive bubble growth (oversaturation degassing) occurs at a constant pressure when a magma finds itself oversaturated in volatiles. Volatile mass is added to bubbles, but the solubility of the volatile in the melt remains constant (constant pressure) as exsolution leads toward chemical equilibrium. Diffusive bubble growth is irreversible.

2. Decompressive bubble growth is a physical and chemical equilibrium response to decompression. It includes two parts. The first is simple expansion of a bubble with constant mass. The second is the mass added to the bubble in response to the reduction in solubility in order to maintain chemical equilibrium during "infinitely slow" decompression. Decompressive bubble growth (both parts) is reversible because thermodynamic equilibrium is always maintained.

Actual magmas experience a combination of diffusive and decompressive bubble growth during their degassing histories. The relative contribution of the two at any instant in time can be characterized by a decompression factor given by the ratio of decompressive to diffusive bubble growth rates integrated over the time of bubble growth.

Water was the only volatile considered in the model for rhyolitic and basaltic magmas. The effects of dissolved water on magma properties are relatively well studied as it is the most common dominant volatile. We did not include CO_2 because variations of magma properties (viscosity, diffusivity, etc.) as a function of CO_2 concentration have

Table 1. The Analytical System of Equations

Process	Equation	Equation
Hydrodynamics of melt surrounding the bubble[a]	$p_g - p_f = \frac{2\sigma}{R} - 4 \nu_R R^2 \int_{z(R)}^{z(S)} \eta(z)\, dz$	(A9)
Mass balance at the bubble interface[b]	$d\left(\frac{P_g R^3}{T_g}\right) = 3 \frac{B}{M} R^2 D \rho \left(\frac{\partial x}{\partial r}\right)_{r=R} dt$	(A12)
Volatile diffusion in the melt	$\frac{\partial x}{\partial t} + v_r \frac{\partial x}{\partial r} = \frac{1}{r^2} \frac{\partial}{\partial r}\left(D r^2 \frac{\partial x}{\partial r}\right)$	(A14)
boundary and initial conditions:		(A15a)
initially uniform volatile distribution	$x(r,0) = x_0 \quad r > R \quad t = 0$	
impermiability of outer cell border	$\left(\frac{\partial x}{\partial r}\right)_{r=S} = 0 \quad t > 0$	(A15b)
Henry's law of gas solubility on the bubble interface	$x(R,t) = x_R = \left(K_h p_g\right)^{1/n} \quad r = R \quad t > 0$	(A15c)
Heat balance at the bubble interface and within it[c]	$\frac{dT_g}{dt} = \frac{3 B T_g}{p_g R c_P M}\left[\rho c_m \chi \left(\frac{\partial T}{\partial r}\right)_{r=R} - \frac{\Delta H_{ev}}{M} D \rho \left(\frac{\partial x}{\partial r}\right)_{r=R} + \frac{R}{3}\frac{dp_g}{dt}\right]$	(A22)
Temperature diffusion in the melt, generation of dissipative and vitrification heating	$\frac{\partial T}{\partial t} + v_r \frac{\partial T}{\partial r} = \frac{1}{r^2}\frac{\partial}{\partial r}\left(\chi r^2 \frac{\partial T}{\partial r}\right) + 12 \frac{\nu}{c_m} v_R^2 \frac{R^4}{r^6} - \left(\frac{H'_{vt}}{c_m}\frac{dT}{dt}\right)_{T<T_{vt}}$	(A26)
boundary and initial conditions:		(A27a)
initially uniform temperature distribution	$T(r,0) = T_0 \quad r \geq R \quad t = 0$	
impermiability of outer cell border	$\left(\frac{\partial T}{\partial r}\right)_{r=S} = 0 \quad t > 0$	(A27b)
bubble interface temperature	$T(R,t) = T_g \quad r = R \quad t > 0$	(A27c)
Viscosity[d]	$\eta = \eta' \exp\left(\frac{E_\eta^{dry}\left(1 - k_\eta x_{volatile}\right)}{B T}\right)$	(A30)
Volatile diffusivity[e]	$\ln D_{water} = \ln x - b - \frac{E_D}{B T}$	(A33)
Heat of (water) vaporization[f]	$\Delta H_{ev} = \sum_{i=0}^{5}\left[(\ln P)^i \sum_{j=0}^{2} k_{j,i} T^i\right]$	(A36)
Ambient pressure[g]	$p_f = \rho g \left(h_0 - v_h t\right)$	

See Table A1 for notations.
[a]Combined equation of momentum and continuity; $z=1/r^3$; equation (A9) comes to $p_g = p_f + p_\sigma + p_v$.
[b]Diffusive bubble growth.
[c]Includes pdV heat, vaporization heat,, and heat flux from the melt.
[d]As a function of temperature and volatile content within melt profile.
[e]As a function of viscosity within the melt profile.
[f]As a function of temperature and pressure; coefficients $k_{j,i}$ are given in Table A2.
[g]If decompression model is used.

not been investigated in detail. Normally, carbon dioxide is present in the melt only when accompanied by water. Consequently, the coupled effects on all parameters of the system CO_2-H_2O-melt should be taken into account. Unfortunately, very little is known about transport properties of the combined system.

2. Properties of Rhyolitic and Basaltic Melts

There are several properties of magmatic systems which affect bubble growth and therefore control the nature of eruptions. In running our model for both the parametric study as well as the constant decompression study we assigned initial values for parameters on the basis of results from the literature. Some of these values are uncertain, and in many cases, more laboratory and field measurements will be required before they can be constrained more precisely. However, the results of our sensitivity study may provide some insights about which experiments/observations are most critical. As additional data more accurately constrain magmatic parameter values, they can be readily used in our model without changing its structure. The model parameters and their interactions are discussed below.

1. Initial temperature is taken to be slightly higher than the liquidus temperatures of the basaltic and rhyolitic melts at 1 bar. Initial values of all temperature dependent properties such as density, viscosity, etc., are based on this initial temperature.

2. Density of the melt is taken as constant. We assume the melt to be incompressible for all practical purposes. The range of temperature during each model run is too small for thermal expansion effects to be important.

3. Viscosity has a complex dependence on melt composition, volatile content and temperature (equations (A28)-(A30)) through three viscosity parameters: activation energy of dry melt deformation (E_η), a viscosity constant (η') [*Persikov*, 1991], and a volatile correction coefficient (k_η). The viscosity constant is the viscosity as $T \to \infty$ in (A28). The volatile correction coefficient represents the dependence of viscosity on volatile concentration. Measured dry melt viscosity (Table 2) and values for the other constants make it possible to calculate activation energy. However, measurements of the volatile correction coefficient vary significantly. For basaltic melt we used published values for k_η [*Persikov*, 1991]. For rhyolitic melt, the addition of 4-6 wt% of H_2O at 100 MPa and 1100°C has been found to reduce the viscosity of an initially anhydrous melt by 4 orders of magnitude [*Neuville et al.*, 1993; *Persikov*, 1991; *Persikov et al.*, 1990]. The approximation in (A29) is valid only for water concentrations below the dissociation limit [*Silver et al.*, 1990]. For higher water concentrations a two-step formulation is necessary to include the effect of molecular water. A recently published empirical viscosity model for hydrous leucogranitic melts [*Hess and Dingwell*, 1996] was used in this study for rhyolitic systems.

4. Diffusivity of water in silicate melt has a complex dependence on melt composition, volatile content, and temperature. Experimental measurements of diffusivity have focused on molecular species. However, total water diffusion coefficients must be used in the governing equations (Table 1). Evaluation of the latter requires the calculation of water dissociation in magmatic melts. Having done this for both rhyolitic and basaltic melts, we have obtained curves by simple regression for total water diffusion coefficients. Apparent diffusion activation energy (E_D) and the free coefficient (b) have been identified from the curves.

5. Thermal diffusivity was calculated from published values of thermal conductivity of diopside melt [*Carrigan and McBirney*, 1997; *Snyder et al.*, 1994, 1997], in which diopside melt was demonstrated to be an analog of basaltic melt. Despite the known very slight compositional dependence of thermal diffusivity we used the proportional difference between conductivities of rhyolitic and basaltic glass to calculate thermal diffusivity of rhyolitic melt, where $\kappa_{rhyolite}/\kappa_{basalt} = 0.857$ [*Ammar et al.*, 1983].

6. Surface tension of the melt is considered constant in our numerical simulations [*Proussevitch et al.*, 1993]. Values for melts with low dissolved water contents are tabulated in Table 2.

7. Heat capacity of superheated water vapor is taken from experimental measurements [*Perry et al.*, 1984]. Most of the heat in the system is stored in the melt, and the temperature within bubbles is mainly governed by the heat flux from the melt. We assume constant water vapor heat capacity in the numerical model at values appropriate for the final P-T conditions of numerical runs because it is at this point that water vapor mass is at a maximum. We use published values for heat capacity of magmatic melts [*Neuville et al.*, 1993; *Richet and Bottinga*, 1986]

8. Heat of vitrification and vitrification temperature have been reliably estimated only for rhyolitic melts [*Neuville et al.*, 1993; *Richet and Bottinga*, 1984, 1986]. Heat of vitrification is much more difficult to determine for basalt because the vitrification temperature of basaltic melt is much lower than it is for highly silicic melt and is associated with the temperature at which melt viscosity is ~10^{12} Pa s. For basaltic melt this may occur at ~550 K, which is unattainable without crystallization unless exceedingly rapid quenching occurs, in which case calorimetric measurements are rendered impossible. Consequently, given the lack of experimental data for basaltic melt, we use related estimates for the system albite-anorthite-diopside [*Stebbins et al.*, 1984].

9. Vitrification interval is the range of temperature over which melt converts to glass and has not been studied for magmatic melts. We expect the range to be wider for faster quench rates and have arbitrarily selected values for both rhyolitic and basaltic melts. The vitrification interval for rhyolite composition is taken as twice that of basalt in analogy to the crystallization intervals (between liquidus and solidus) for these melts.

3. Parametric Study

In the interactive parametric bubble growth model, a change of any parameter affects all other parameters which collectively govern the dynamics of the bubble growth and volatile exsolution. For example, the change of dissolved

Table 2. Properties of Rhyolitic and Basaltic Magmas and Other Constants Used in the Numerical Simulations

Symbol	Property	Value	Units	Reference
		Rhyolitic Melt		
T_0	temperature	1273	K	specified
ρ	density	2200	kg m^{-3}	[*Clark et al.*, 1987]
η	viscosity of dry melt	10^8	Pa s	[*Hess and Dingwell*, 1996]
E_η	activation energy	$3.045\ 10^5$	J $mole^{-1}$	calculated from η
η'	viscosity constant	$10^{-4.5}$	Pa s	[*Persikov*, 1991]
k_η	volatile correction	11.0	none	calculated
D_{H_2O}	diffusivity, x=0.002	$1.8\ 10^{-12}$	$m^2\ s^{-1}$	calculated
E_D	activation energy	87300	J $mole^{-1}$	calculated
b	coefficient for diffusivity	12.574	none	calculated
χ	temperature diffusivity	$1.42\ 10^{-7}$	$m^2\ s^{-1}$	[*Snyder et al.*, 1994]
K_h	henry constant	$1.6\ 10^{-11}$	Pa^{-1}	[*Burnham*, 1975]
σ	surface tension	0.32	N m^{-1}	[*Proussevitch and Kutolin*, 1986]
c_m	heat capacity of melt	$1.35\ 10^3$	J kg^{-1} K^{-1}	[*Neuville et al.*, 1993]
c_P	heat capacity of H_2O	$2.50\ 10^3$	J kg^{-1} K^{-1}	[*Perry et al.*, 1984]
ΔH_{vt}	heat of vitrification	$7.15\ 10^3$	J kg^{-1}	[*Neuville et al.*, 1993]
T_{vt}	vitrification temperature	1075	K	[*Bacon*, 1977]
ΔT_{vt}	vitrification interval	50	K	specified
		Basaltic Melt		
T_0	temperature	1473	K	specified
ρ	density	2600	kg m^{-3}	[*Murase and McBirney*, 1973]
η	viscosity of dry melt	50	Pa s	[*Shaw et al.*, 1968]
E_η	activation energy	$1.75\ 10^5$	J $mole^{-1}$	calculated from η
η'	viscosity constant	$10^{-4\,5}$	Pa s	[*Persikov*, 1991]
k_η	volatile correction	6.0	none	calculated from D
D_{H_2O}	diffusivity, x=0.002	$1.175\ 10^{-9}$	$m^2\ s^{-1}$	calculated
E_D	activation energy	15200	J $mole^{-1}$	calculated
b	coefficient for diffusivity	12.49	none	calculated
χ	temperature diffusivity	$1.14\ 10^{-7}$	$m^2\ s^{-1}$	[*Snyder et al.*, 1994]
K_h	henry constant	$9\ 10^{-12}$	Pa^{-1}	[*Burnham*, 1975]
σ	surface tension	0.36	N m^{-1}	[*Proussevitch and Kutolin*, 1986]
c_m	heat capacity of melt	$1.45\ 10^3$	J kg^{-1} K^{-1}	[*Richet and Bottinga*, 1986]
c_P	heat capacity of H_2O	$2.65\ 10^3$	J kg^{-1} K^{-1}	[*Perry et al.*, 1984]
ΔH_{vt}	heat of vitrification	$1.2\ 10^5$	J kg^{-1}	[*Stebbins et al.*, 1984]
T_{vt}	vitrification temperature	910	K	[*Stebbins et al.*, 1984]
ΔT_{vt}	vitrification interval	20	K	specified
		Common Constants and Parameters		
B	gas constant	8.31	J $mole^{-1}$ K^{-1}	general constant
g	gravity acceleration	9.81	m s^{-2}	general constant
ΔH_{ev}	vaporization heat[a]	$2.023\ 10^5$	J $mole^{-1}$	[*Sahagian and Proussevitch*, 1996]
M_{H_2O}	molecular weight of water	$18\ 10^{-3}$	kg $mole^{-1}$	general constant
M_{CO_2}	mollecular weight of CO_2	$44\ 10^{-3}$	kg $mole^{-1}$	general constant
R_o	initial bubble radius	10^{-5}	m	Used for decompression runs
S_o	bubble separation	10^{-3}	m	Used for decompression runs

Properties at 0.1 MPa.
[a]Water at 1273 K

water concentration associated with degassing causes changes in system temperature, viscosity, diffusivity, etc. It follows that a parametric study of the present interactive model will not reveal the effect of each parameter independently of all others. Instead, it highlights the effect of variation of the initial values of each parameter during a model run in which all parameters are interdependent and allowed to evolve as they do in natural systems.

The analytical system of governing equations (see Table 1) involves 11 interacting variables, each of which can be explored as a function of time in the parametric study. In addition, there are 23 constants in the system of

Table 3. The Standard Set of Parameters for Both Basaltic and Rhyolite Compositions Used in Numerical Experiments of Parametric Study

Melt	Volcanic System Parameters Other Than Melt Properties						Major Melt Properties From Table 2					
	x_0,	p_f, MPa	T_0, K	R_0 x 10^5, m	S_0 x 10^3, m	Fluid	η_0, Pa s	D_0 x 10^{11}, m^2 s^{-1}	c x 10^7, m^2 s^{-1}	ΔH_{ev} x 10^{-5}, J $mole^{-1}$	ΔH_{vt} x 10^{-3}, J kg^{-1}	T_{vt}, K
Rhyolite	1.0	0.1	1273	1.0	1.0	H_2O	4 10^6	0.9	1.42	2.02	7.15	1075
Basalt	0.5	0.1	1473	1.0	10.0	H_2O	50	1 103	1.14	2.02	120	910

equations (Table 1). Most are properties of the melt and other constants listed in Table 2. Many of the parameters are linked in that a variation of one causes a variation of another (i.e. volatile content and viscosity, or viscosity and diffusivity, etc.). These secondary variations are allowed to occur in the parametric study as specified by the formulation summarized in Table 1 (in contrast to the more restrictive approach of *Proussevitch et al.* [1993]. Thus our externally applied variation of the initial value of each parameter affects the evolution of other parameters and we allow all variables to change with time during the model runs. We varied each parameter from a standard set of initial parameters we have defined for our model "basaltic" and "rhyolitic" systems (Table 3).

The present parametric study focuses on rhyolitic melt because the results for basaltic melts are very similar to

Table 4. List of Model Runs in Parametric Study, Variation of Parameters, and Major Results

File	Parameter(s) Different Than in Standard Set	Major Results												
		t_{final},[a] s	t_{delay}, s	t_{disr},[b] s	Δc_{disr},[c] wt%	R_0/R_{cr}	R_{final}, mm	Δp_{max},[d] MPa	$\frac{\eta_{max}}{\eta_{min}}$[e]	lg η_{st} [f] Pa s	lg η_{fn} [f] Pa s	ΔT_{dis}, K	ΔT_{vap}, K	ΔT_{pdv}, K	T_{final}, K
	Rhyolite Series of Model Runs														
rhy-st	standard set	393.0	99.54	151.7	0.77	96.1	4.83	3.69	15.1	6.62	7.85	0.74	-3.72	-0.78	996.3
rhy-r1	bubble radius R_0=1.041 10^{-7} m	434.0	129.1	187.5	0.77	1.0003	4.83	5.46	15 4	6.62	7.85	0.69	-3.71	-0.70	996.3
rhy-r2	bubble radius R_0=1.051 10^{-7} m	423.8	120.2	177.9	0.77	1 01	4.83	5.46	15.4	6.62	7.85	0.69	-3.71	-0.70	996.3
rhy-r3	bubble radius R_0=1.072 10^{-7} m	419.1	117.0	173.4	0.77	1.03	4.83	5.46	15.3	6.62	7.85	0.70	-3.71	-0.70	996.3
rhy-r4	bubble radius R_0=1.145 10^{-7} m	414.6	114.3	171.5	0.77	1 10	4.83	5.47	15.4	6.62	7.85	0.69	-3.71	-0.70	996.3
rhy-r5	bubble radius R_0=1.04 10^{-6} m	404.6	104.4	159.1	0.77	9.99	4.83	5.47	15.3	6.62	7.85	0.70	-3.71	-0.72	996.3
rhy-s1	bubble separation S_0=5.0 10^{-5} m	77.10	10.52	22.16	0.29	96.1	0.24	3.61	1.07	6.62	7.87	8.09	-5.00	-8.70	994.6
rhy-s2	bubble separation S_0=1.0 10^{-4} m	87.14	20.98	34.15	0.43	96.1	0.48	3.64	1.86	6.62	7.87	6.53	-4.87	-6.95	994.9
rhy-s3	bubble separation S_0=5.0 10^{-4} m	177.7	70.58	94.70	0.71	96.1	2.41	3.64	12.3	6.62	7.86	1.83	-4.04	-1.91	995.9
rhy-s4	bubble separation S_0=5.0 10^{-3} m	6252	206.7	740.6	0.80	96.1	24.1	3.71	16.3	6.62	7.85	0.07	-3.50	-0.07	996.5
rhy-s5	bubble separation S_0=1.0 10^{-2} m	24156	397.7	2161	0.80	96.1	48.3	3.72	16.3	6.62	7.85	0.02	-3.48	-0.02	996.5
rhy-c1	concentration c=0.5 wt% H_2O	1944	623.6	1055	0.28	22.9	3.64	1.27	3.03	7.31	7.83	0.32	-1.60	-0.33	998.4
rhy-c2	concentration c=2.0 wt% H_2O	80.61	9.780	15.61	1.77	389	6.22	5.28	399	5.25	7.89	1.00	-7.80	-1.04	992.2
rhy-c3	concentration c=3.0 wt% H_2O	36.79	4.289	6.321	2.76	877	7.17	5.61	10733	3.87	7.93	1.37	-11.9	-1.41	988.2
rhy-c4	concentration c=4.0 wt% H_2O	22.42	3.456	4.550	3.73	1561	7.91	6.57	2.9 10^5	3.30	7.97	2.03	-16.0	-2.10	984.2
rhy-c5	concentration c=5.0 wt% H_2O	15.24	2.737	3.380	4.69	2440	8.53	7.60	7.7 10^6	2.81	8.01	2.84	-20.2	-2.94	980.2
rhy-p1	pressure p=0.1 MPa, Δc=1.0 %	297.5	68.22	104.5	0.89	122	5.05	4.01	22.8	6.45	7.86	0.80	-4.25	-0.84	995.7
rhy-p2	pressure p=1.0 MPa, Δc=1.0 %	18.27	49.79	872.7	0.30	176	2.34	4.24	23.1	6.07	7.50	0.03	-5.83	-0.04	994.2
rhy-p3	pressure p=10.0 MPa, Δc=1.0 %	11468	263.8	-	-	345	1.09	1.45	22.9	4.88	6.30	0.00	-5.55	0.00	994.5
rhy-p4	pressure p=50.0 MPa, Δc=1.0 %	24576	453.4	-	-	650	0.636	0.407	20.6	2.73	4.12	0.00	-3.26	0.00	996.8
rhy-p5	pressure p=100 MPa, Δc=1.0 %	29476	498.2	-	-	879	0.505	0.009	19.4	1.12	2.50	0.00	-1.83	0.00	998.2
rhy-t1	temperature T= 900°C	1788	661.4	931.1	0.70	96.1	4.70	4.57	14.9	7.57	8.92	1.84	-4.70	-1.91	895.3
rhy-t2	temperature T= 950°C	766.6	247.2	358.1	0.74	96.1	4.76	4.10	15.6	7.07	8.37	1.16	-4.17	-1.21	945.8
rhy-t3	temperature T= 1050°C	228.6	41.47	69.91	0.78	96.1	4.89	3.05	14.1	6.20	7.38	0.48	-3.37	-0.50	1046.6
rhy-t4	temperature T=1100°C	147.4	18.51	34.84	0.79	96.1	4.95	2.85	13.0	5.81	6.94	0.32	-3.09	-0.34	1096.9
rhy-v1	viscosity E_η=200 kJ $mole^{-1}$ k_η=7	222.3	3.100	18.28	0.80	96.1	4.82	0.28	3.17	3.13	3.65	0.00	-3.47	-0.00	996.5
rhy-v2	viscosity E_η=250 kJ $mole^{-1}$ k_η=9	234.4	5.099	22.97	0.80	96.1	4.83	1.21	6.45	4.83	5.67	0.03	-3.49	-0.03	996.5
rhy-v3	viscosity E_η=350 kJ $mole^{-1}$ k_η=12	5227	1266	2040	0.54	96.1	4.83	5.62	5.21	8.14	9.70	5.39	-4.73	-5.58	995.2
rhy-d1	diffusivity E_D=50 kJ $mole^{-1}$	104.7	37.72	54.35	0.57	96.1	4.83	5.60	4.53	6.62	7.87	4.90	-4.65	-5.07	995.3
rhy-d2	diffusivity E_D=75 kJ $mole^{-1}$	199.5	71.98	104.1	0.73	96.1	4.83	4.39	13.2	6.62	7.86	1.58	-3.97	-1.64	996.0
rhy-d3	diffusivity E_D=100 kJ $mole^{-1}$	993.7	121.6	241.3	0.79	96.1	4.83	2.83	15.9	6.62	7.85	0.32	-3.59	-0.33	996.4
rhy-d4	diffusivity E_D=125 kJ $mole^{-1}$	8481	244.5	939.7	0.80	96.1	4.83	1.44	16.1	6.62	7.85	0.05	-3.49	-0.06	996.5

Table 4. (continued)

File	Parameter(s) Different Than in Standard Set	Major Results													
		t_{final},[a] s	t_{delay}, s	t_{disr},[b] s	Δc_{disr},[c] wt%	R_0/R_{cr}	R_{final}, mm	Δp_{max},[d] MPa	$\frac{\eta_{max}}{\eta_{min}}$[e]	lg η_{st} [f] Pa s	lg η_{fn} [f] Pa s	ΔT_{dis}, K	ΔT_{vap}, K	ΔT_{pdv}, K	T_{final}, K
Basalt Series of Model Runs															
bas-st	standard set	54.86	n.a.	6.445	0.35	37.2	41.50	0.519	1.42	1.52	1.67	0.00	-1.14	0.00	1198.9
bas-s1	bubble separation S_0= 1.0 10^{-4} m	0.007	n.a.	0.002	0.34	37.2	0.412	0.531	1.41	1.52	1.67	0.31	-1.20	-0.15	1198.8
bas-s2	bubble separation S_0= 1.0 10^{-3} m	0.554	n.a.	0.073	0.35	37.2	4.15	0.537	1.41	1.52	1.67	0.00	-1.15	0.00	1198.9
bas-s3	bubble separation S_0= 5.0 10^{-3} m	13.65	n.a.	1.634	0.35	37.2	20.75	0.561	1.42	1.52	1.67	0.00	-1.14	0.00	1198.9
bas-s4	bubble separation S_0= 5.0 10^{-2} m	1358	n.a.	162.8	0.35	37.2	207.5	0.532	1.42	1.52	1.67	0.00	-1.14	0.00	1198.9
bas-c1	concentration c=0.25 wt% H_2O	260.4	n.a.	71.26	0.10	8.26	30.15	0.189	1.14	1.61	1.67	0.00	-0.44	0.00	1199.6
bas-c2	concentration c=1.0 wt% H_2O	13.55	n.a.	0.755	0.85	153	54.26	1.13	2.19	1.33	1.68	0.00	-2.55	0.00	1197.5
bas-c3	concentration c=1.5 wt% H_2O	5.736	n.a.	0.221	1.35	346	62.76	1.56	3.36	1.15	1.68	0.00	-3.95	0.00	1196.1
bas-c4	concentration c=2.0 wt% H_2O	3.236	n.a.	0.089	1.85	616	69.46	1.81	5.22	0.96	1.69	0.00	-5.35	0.00	1194.7
bas-c5	concentration c=3.0 wt% H_2O	1.338	n.a.	0.027	2.85	1388	79.87	2.17	12.4	0.59	1.70	0.00	-8.12	0.00	1191.9
bas-p1	pressure p=0.1 MPa, Δc=1.0 %	11.44	n.a.	0.571	0.95	184	56.10	1.22	2.39	1.30	1.68	0.00	-2.82	0.00	1197.2
bas-p2	pressure p=1.0 MPa, Δc=1.0 %	118.5	n.a.	40.94	0.49	245	26.01	1.07	2.37	1.22	1.61	0.00	-4.89	0.00	1195.1
bas-p3	pressure p=10.0 MPa, Δc=1.0 %	840.3	n.a.	-	-	447	12.08	0.384	2.37	0.98	1.37	0.00	-4.64	0.00	1195.4
bas-p4	pressure p=50.0 MPa, Δc=1.0 %	2020	n.a.	-	-	809	7.06	0.123	2.30	0 54	0.92	0.00	-2.60	0.00	1197.4
bas-p5	pressure p=100 MPa, Δc=1 0 %	2577	n.a.	-	-	1080	5.61	0.044	2.26	0 22	0.59	0.00	-1.44	0.00	1198.6
bas-t1	temperature T = 1100°C	64.59	n.a.	8.270	0.35	37.2	40.54	0.714	1.45	1.96	2.12	0.00	-1.28	0.00	1098.7
bas-t2	temperature T = 1300°C	46.12	n.a.	5.236	0.36	37.2	42.42	0.434	1.38	1.14	1.28	0.00	-1.08	0.00	1298.9
bas-v1	viscosity E_η=150 kJ mole^{-1} k_η=5	54.78	n.a.	6.488	0.35	37.2	41.50	0.266	1.28	0.69	0.80	0.00	-1.14	0.00	1198.9
bas-v2	viscosity E_η=200 kJ mole^{-1} k_η=7	55.23	n.a.	6.732	0.35	37.2	41.50	0.951	1.59	2.34	2.55	0.00	-1.14	0.00	1198.9
bas-d1	diffusivity E_D=10 kJ mole^{-1}	35.85	n.a.	4.225	0.35	37.2	41.50	0.072	1.42	1.52	1.67	0.00	-1.14	0.00	1198.9
bas-d2	diffusivity E_D=20 kJ mole^{-1}	81.13	n.a.	9.605	0.35	37.2	41.50	0.472	1.42	1.52	1.67	0.00	-1.14	0.00	1198.9
bas-d3	diffusivity E_D=30 kJ mole^{-1}	180.9	n.a.	21.62	0.35	37.2	41.50	0.358	1.42	1.52	1.67	0.00	-1.14	0.00	1198.9

[a]Time defined at 99 % of final bubble radius.
[b]Fragmentation threshold is taken at 90 % of gas volume in the system.
[c]Average melt oversaturation at fragmentation.
[d]Dynamic pressure term.
[e]Average viscosity ratio within the melt at time of 50% of final bubble radius. According to (A33) the same ratio is for diffusivity.
[f]Average melt viscosity across the bubble wall.

those of *Proussevitch et al.* [1993]. This is because bubble growth in basaltic melts is limited only by volatile diffusion as viscous relaxation is relatively rapid in the low viscosity melt. Nevertheless, we have included the results of a few basaltic model runs in Table 4 for comparison with the rhyolite runs.

3.1. Initial Bubble Radius and Time Delay of Bubble Growth

Model results for bubble growth in rhyolitic melt with our standard set of parameters (Table 2) with variations of the initial bubble radius (Table 4) describe a sigmoidal bubble growth curve (Figure 2a). These curves have flatter early and late phases than the corresponding results of the isothermal model [*Proussevitch et al.*, 1993]. Time delay was further discussed and explained in [*Sahagian et al.*, 1994; *Sparks*, 1994].

The dynamic bubble growth curves of our model can be compared with those of the "classical" analytical formulation of bubble growth in infinite media [*Epstein and Plesset*, 1950; *Rosner and Epstein*, 1972; *Scriven*, 1959; *Szekely and Fang*, 1973], which has been applied to volcanology [*Bottinga and Javoy*, 1990; *Sparks*, 1978; *Toramaru*, 1989; *Westrich et al.*, 1988]. The classical model involves a parabolic growth law

$$R \sim t^{1/2} \tag{1}$$

There is no part of the full growth curve shown in Figure 2a which "obeys" the parabolic growth law as there is no linear segment in logarithmic coordinates (Figure 3). Thus the classical law (equation (1)) does not work for any part of bubble growth history with close bubble spacing and interacting parameters. A similar result has been found previously [*Arefmanesh et al.*, 1992].

The initial bubble radius refers to the bubble size at the start of the numerical analysis. The bubble may attain this size after nucleation by various means not explored here, but in the model the initial size controls the time delay before the main phase of bubble growth. *Sparks* [1978] defined the term "time delay" as the interval between nucleation and the time the bubble starts to grow in accordance with the parabolic law (equation (1)). Because our model suggests that the parabolic law does not apply to interactive bubble growth with finite bubble spacing, we can qualitatively interpret the time delay as the time before

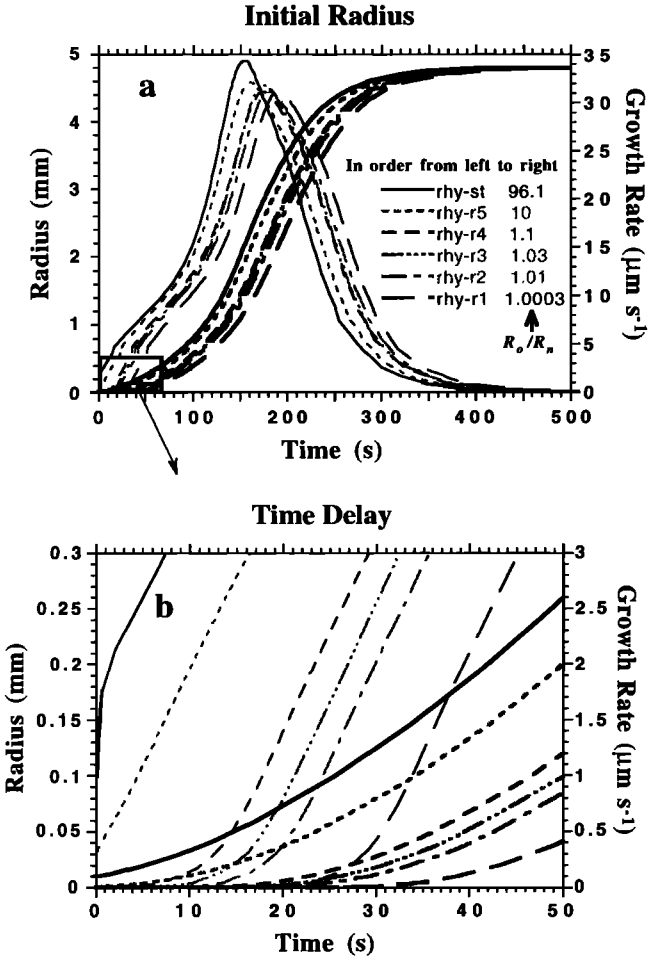

Figure 2. Bubble radius and growth rate in rhyolitic melt for various initial bubble radii. Growth rates are shown as thin lines. Parameters and melt properties are defined in Tables 2 and 3. (a) The curves for the whole growth time interval. (b) Early stages of bubble growth history controlled by initial bubble radius and time delay. The difference between growth lines is produced before the growth rate reaches a common value for all (conformable) curves shown in Figure 2a.

the steep part of the growth curve described below (equation (2)). Because our modeled bubble growth depends on many factors and can only be calculated numerically (no analytical solution), the results can only be described empirically. The best linear approximation (Figure 4) for the important (rapid) part of bubble growth is a logarithmic relation where

$$R \sim \log t \qquad (2)$$

This growth is slower (becomes retarded with time) relative to the "traditional" $t^{1/2}$ parabolic growth because of our introduction of parametric interactions in the model. The influx of volatiles into the bubble becomes slower because of the reduction in diffusivity (2-3 orders of magnitude) due to interacting concentration reduction, temperature decrease, and viscosity increase. If the traditional parabolic growth of bubble radii were plotted on

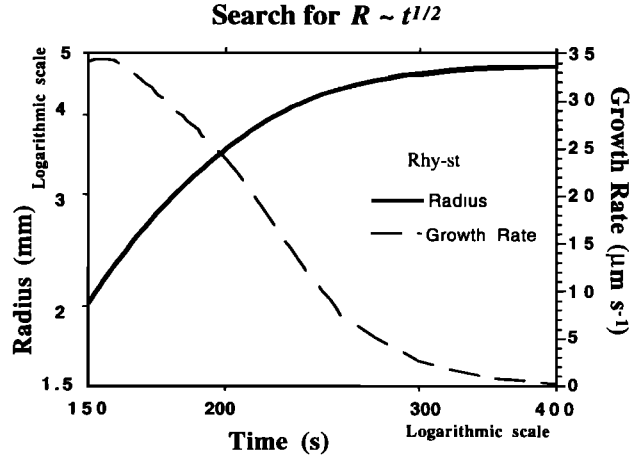

Figure 3. Test of parabolic bubble growth ($R \sim t^{1/2}$), which requires a decrease in growth rate with time. Figure 2a shows that growth rate increases to a maximum, then decreases, so the parabolic "law" can only relate to the portion of bubble growth after the rate maximum. In this case it is necessary to find a straight portion of the bubble growth curve (solid line) during the interval of falling growth rate (dashed line) because the derivative of the logarithmic relation must be linear. However, it is clear that there is no linear portion of the radius curve (solid line) in logarithmic coordinates. This indicates that the $R \sim t^{1/2}$ relation is not valid for any part of bubble growth under conditions of close bubble spacing and realistic interaction between magma parameters. A logarithmic growth law is more appropriate under most conditions but is still not valid in all cases.

Figure 3, it would describe a straight line (note that our results describe a curve with negative second derivative).

We ran five numerical model runs with various initial bubble radii from 0.03% greater than nuclear size to 100

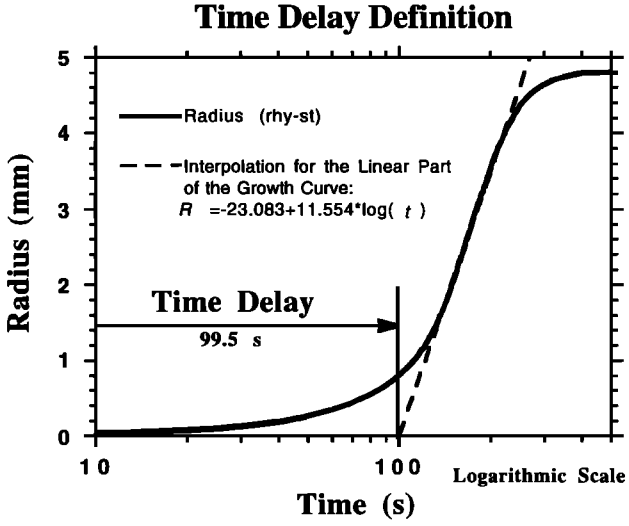

Figure 4. Time delay is defined as the time before bubble growth can be characterized by logarithmic growth $R \sim \log(t)$. The logarithmic dependence is reflected in the linear part of the curve (logarithmic time axis and linear radius axis). To find the time delay, the linear part of the growth curve is extrapolated to the time axis.

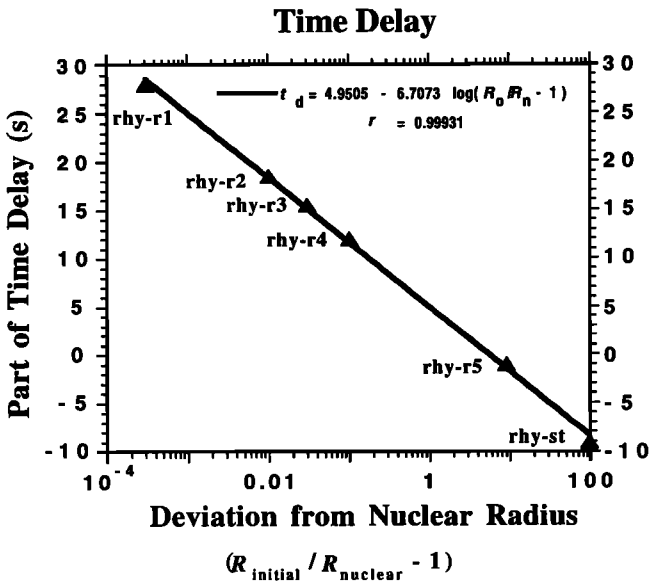

Figure 5. Dependence of total time delay on initial bubble size relative to nuclear size. The first part of the time delay is governed only by initial bubble radius while a separate (dynamic) part depends on melt properties.

times nuclear size (rhy-r1 to rhy-r5 and rhy-st) (Figure 2). There is a large time delay due to the initial volatile oversaturation and transport properties of the melt (viscosity, diffusivity, and surface tension) and an additional contribution from the initial bubble radius. The latter shifts the growth curve along the time axis and leads to what we can call a "radius time delay." We can examine the radius time delay for the early part of the growth history plotted on Figure 2b by extrapolation of the straight segment of the curve to the time axis. From a plot of the radius time delay versus deviation from nuclear radius (R_0/R_n-1) an empirical relation is revealed (Figure 5) in the form of

$$t_{delay} = a - b \log_{10}\left(\frac{R_{initial}}{R_{nuclear}} - 1\right) \quad (3)$$

where a and b are positive coefficients. In the case of rhyolite (Table 2) the coefficients are 4.95 and 6.71, respectively, and correlation coefficient for (3) is $r = 0.99931$ (Figure 5). Thus, for bubbles close to nuclear size the radius time delay could be up to 30-50 s which could extend the total time of bubble growth by ~10%. Another interesting aspect of the radius time delay is that it can be negative if the initial bubble radius is much larger than nuclear size so that rapid initial growth is allowed by high volatile concentration at and near the bubble interface without large counteracting surface tension. Bubble growth rate reflects the volatile concentration gradient in the surrounding magma (Figure 2b). The time delay is defined as the time elapsed before the constant growth rate is reached. In most cases, there is a positive time delay caused by the inability of oversaturated volatiles to enter very small bubbles (with very small surface areas) [*Proussevitch et al.*, 1993]. However, excessive concentration gradients can overcome the geometrical limitation, leading to rapid initial growth before reaching a quasi-equilibrium rate.

3.2. Bubble Separation

Bubble separation is reflected in our model as the radius of the outer border of the elementary bubble cell. The center-to-center distance between neighboring bubbles is twice this length. Bubble separation is also related to bubble number density in the magma. Bubble separation plays an important role in bubble growth dynamics because it determines the volume of melt associated with each bubble from which the bubble can draw volatiles for diffusive growth and against which the bubble must exert forces to displace melt during growth.

Bubble separation is controlled by a nucleation process such that additional nucleation decreases bubble separation and can lead to a complex bubble size distribution in natural systems. We do not explore nucleation processes here but assign a single initial bubble separation to describe the system.

We ran a suite of model runs (Table 4) on the basis of a standard set of parameters (Table 3) in which we varied bubble separation (measured by S_0/R_0) from 5 to 1000. The results reveal a strong dependence of final bubble growth time on bubble separation. This time is roughly proportional to the square root of the volume of the shell of melt surrounding the bubble. The final bubble radius is directly proportional to melt shell volume.

Figure 6 demonstrates that bubble growth history (radius) is relatively independent of bubble separation (overlying curves) until all gas is exsolved. Qualitatively, this result is the same as that of the isothermal,

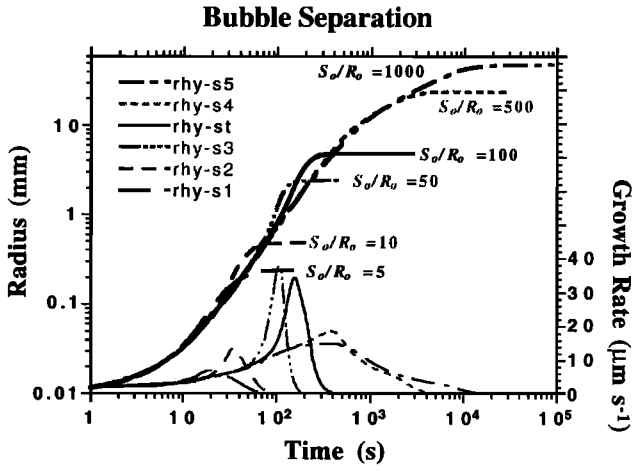

Figure 6. Bubble growth in rhyolitic melt for different values of initial bubble separation from 0.05 mm to 1 cm with constant initial bubble radius of 0.01 mm. Growth rate curves are shown as thin lines. It is evident that bubble growth does not depend strongly on bubble separation until the final stages. Only the volume of melt in the unit cell and volatile concentration (available for exsolution) limit final bubble radius. Thus we can use average bubble separation or bubble number density to characterize a large gas-melt system and numerically simulate its degassing by application of the bubble growth model for an elementary cell (see also Figure 1).

noninteracting bubble growth model [*Proussevitch et al.*, 1993], thus demonstrating that an arbitrary local distribution of bubble separations in natural magmas can be averaged to characterize the system, thus allowing application of the individual bubble growth model to volcanic systems as if there was a single, spatially invariant initial number density.

There are no linear sections on Figure 6 in the descending portions that correspond to power law growth of power <1, but linear segments are observed in the ascending portions in the growth rate curve, indicating a power law with power >1 characterized by $R \sim t^{1.45}$ for these intervals. The relationship between the total duration of bubble growth and initial cell size S_0 can be approximated by the same power dependence $t_{final} \sim S_0^{1/1.45}$. In detail, the best characterization of the bubble growth curves (aside from initial and final stages) is logarithmic as shown by (2). For the case of bubble separation all curves overlap (Figure 6) because the dynamics of bubble growth do not depend on separation until later stages of growth (when bubbles "feel" the presence of neighboring bubbles), and we can describe the composite curve as

$$R(\text{mm}) = 31.4 \log(t(\text{s})) - 83.2 \quad (4)$$

3.3. Initial Water Concentration in the Melt

The dissolved volatile content of degassing magma plays an important role in controlling eruption dynamics [*Eichelberger and Westrich*, 1981; *Neri and Dobran*, 1994; *Sahagian and Anderson*, 1991; *Wilson*, 1980]. In order to examine its effect we conducted six model runs with various initial dissolved volatile concentrations from 0.5 to 5 wt% H_2O at atmospheric pressure (Table 4). We chose 1 bar because it is in the vent and shallow conduit where the most rapid degassing often takes place in highly silicic systems. The bubble growth curves are plotted in Figure 7. The analysis is complex because the amount of cooling (and consequent changes in melt properties) is controlled by the amount of water vaporization. For water oversaturation >~3 wt% and initial temperature of 1000°C the melt cools by ~25 K.

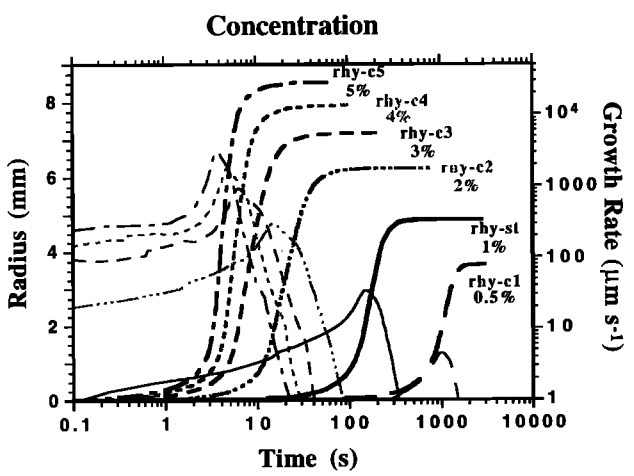

Figure 7. Bubble growth in rhyolitic melt for various volatile concentrations from 0.5 to 5 wt% H_2O instantaneously decompressed to atmospheric pressure. Growth rate curves are shown as thin lines. In general, greater volatile oversaturation leads to faster bubble growth. However, for high water content (>3 wt%) the process is complicated by significant system cooling as temperature approaches the vitrification point. Vitrification stops bubble growth and arrests melt oversaturation, making it independent of initial water content. During active bubble growth the growth rates vary by 3 orders of magnitude depending on volatile concentration.

Bubble growth rate, time delay, and total growth time vary by 3 orders of magnitude for a tenfold variation in initial dissolved water concentration (Figure 7). Our model results reveal empirical dependencies of these quantities on initial volatile content such that

$$v_R \sim x_{water}^{3} \quad t_{delay} \sim x_{water}^{-3} \quad t_{final} \sim x_{water}^{-2} \quad (5)$$

where v_R refers to the maximum observed bubble growth rate. Clearly, dissolved water content controls bubble growth dynamics, as was determined as a result of the simple, noninteracting, isothermal model [*Proussevitch et al.*, 1993]. However, the interactions between melt properties lead to a stronger modeled control of growth dynamics because viscosity is lower and diffusivity is greater for melts with higher water contents, so that initial water concentration plays a more important role when magma parameter interactions are taken into account. Thus a seemingly paradoxical situation arises where a rhyolitic melt with 5 wt% water can degas much faster (few seconds) than one with 0.5 wt% water, even though the water content of the former must at some point become the 0.5 wt% of the latter before degassing is completed. The cause of this is the larger bubbles and thus thinner walls (diffusion distances) for the 5 wt% case at low pressures.

3.4. Ambient Pressure

In our parametric study we took ambient pressure to be the pressure to which an initially saturated magma is instantaneously decompressed, leading to oversaturation. Conceptually, this is a case of complete oversaturation degassing [*Sahagian and Proussevitch*, 1996] where the initially oversaturated melt suddenly finds itself at a fixed lower pressure and degasses as a result of the sudden oversaturation. We varied ambient pressure from atmospheric to 100 MPa (Figure 8). Although we would like to separate the effects of variations of each melt parameter individually as done previously [*Proussevitch et al.*, 1993], it is unrealistic to discount the interaction of ambient pressure with volatile solubility. Therefore, in the numerical runs with different ambient pressures (rhy-p1-p5, see Table 4), initial dissolved water content was adjusted so that initial water oversaturation could be the same (1 wt%) for all model runs, providing a more useful comparison than the case where the main bubble growth dynamics were driven primarily by differences in oversaturation. One might expect that degassing should be slower at higher pressures because the necessary diffusion distance is greater because of smaller (compressed) bubbles and large "wall thicknesses." However, the

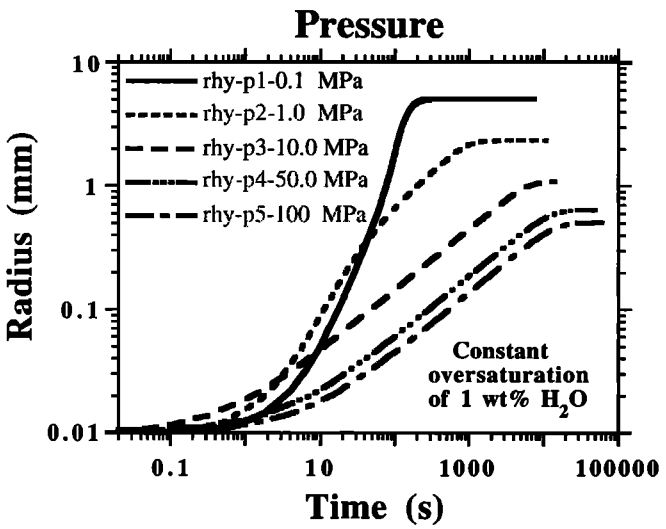

Figure 8. Bubble growth in rhyolitic melt for different values of ambient pressure between 0.1 and 100 MPa in the interacting parametric model. Initial volatile (water) oversaturation is 1 wt% for all runs. Unlike the earlier noninteracting model [*Proussevitch et al.*, 1993], degassing and bubble growth is not faster for model runs with instantaneous decompression to lower ambient pressures. Instead, high total water content (not oversaturation) at high pressures makes viscosity much lower and diffusivity much greater than at low pressures which compensates for the effect of greater diffusion distance associated with smaller bubbles at high ambient pressure. Thus bubble growth is relatively insensitive to ambient pressure.

numerical model revealed that bubble growth is insensitive to ambient pressure, especially at high pressures (Figure 8). This is because water solubility is greater at high pressures, causing a reduction in melt viscosity and an increase in diffusivity. The higher diffusivity compensates for the greater diffusion distances at high pressure. This result cannot be assessed in the parametric study but emerges in the full interactive bubble growth model as described below in section 4. For our "standard" conditions (Tables 2 and 4), exsolution of 1 wt% H_2O is completed within ~15 min at low pressures and ~1-2 hours at high pressures.

At high pressures (>10 MPa) the period of active bubble growth (straight segments on Figure 8) fits the traditional $R \sim t^{1/2}$ growth law. This result is expected because at high pressures our model conditions are close to those upon which the $R \sim t^{1/2}$ growth law is based [*Scriven*, 1959] where viscosity, diffusivity, and solubility are held constant at the bubble-melt interface and melt advection is ignored. This similarity with the much simpler analysis arises from the fact that at high pressures, there are very small viscosity and diffusivity variations across the bubble wall, and melt advection is minor because of the small final radius of bubbles. However, this is not true at lower pressures, so the $t^{1/2}$ growth law does not hold.

3.5. Temperature

Significant melt temperature variations have been observed in volcanic systems even for similar types of lava [*Melson et al.*, 1990; *Neal et al.*, 1988]. Temperature strongly affects viscosity and diffusivity and thereby affects bubble growth dynamics. In the parametric study for rhyolitic magma we varied temperatures between 900° and 1100°C (Table 4). The results reveal great sensitivity of bubble growth dynamics to temperature. For example, complete bubble growth and melt degassing varied from ~1 min for hot melt to ~1 hour for cold melt (Figure 9). An empirical power law relation emerged from the model results between various bubble growth parameters and temperature such that

$$v_R,\ t_{delay} \sim \Delta T^{-0.5}\ (\mathrm{K})\ . \qquad (6)$$

The sensitivity of bubble dynamics to temperature makes it necessary to consider the thermal effects of degassing which can cause significant changes in melt temperature during exsolution [*Sahagian and Proussevitch*, 1996]. There is a strong feedback between temperature, bubble growth, and degassing which must be accounted for in any realistic model. Temperature can fall by tens of kelvins, leading to contrasting bubble growth dynamics between early and late stages of degassing. However, if significant crystallization occurs, the added latent heat can offset the exsolution cooling. With rapid cooling near the vent during energetic eruptions, crystallization is minimized, and thus it is necessary to consider exsolution cooling but not crystallization in the present model.

3.6. Viscosity

Our numerical model does not use dry melt composition explicitly. Rather, it enters implicitly from dry melt viscosity, which is input directly. Viscosity is introduced in terms of the activation energy of viscous flow (E_η). Numerical runs with different values of activation energy (viscosity) could thus reflect different melt compositions, but we do not define viscosity in terms of composition because there are many variations in composition which

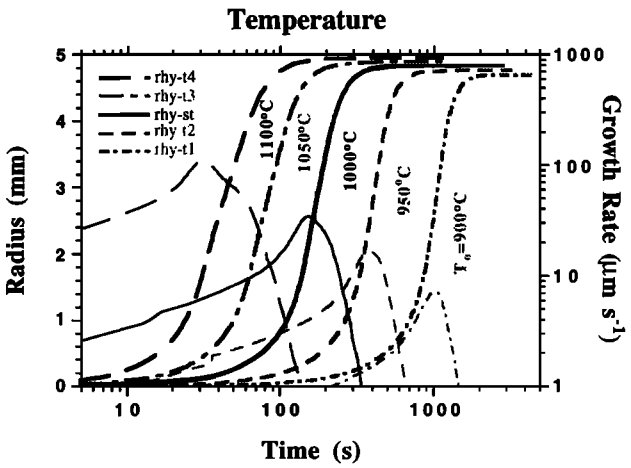

Figure 9. The effect of initial melt temperature on bubble growth in rhyolitic magma. Growth rate curves are shown as thin lines. The variations of temperature cause a logarithmic displacement of the growth curves along the time axis and a small change of final bubble radius due to thermal expansion. Increasing temperature reduces viscosity and increases diffusivity exponentially which leads to the logarithmic response of bubble growth.

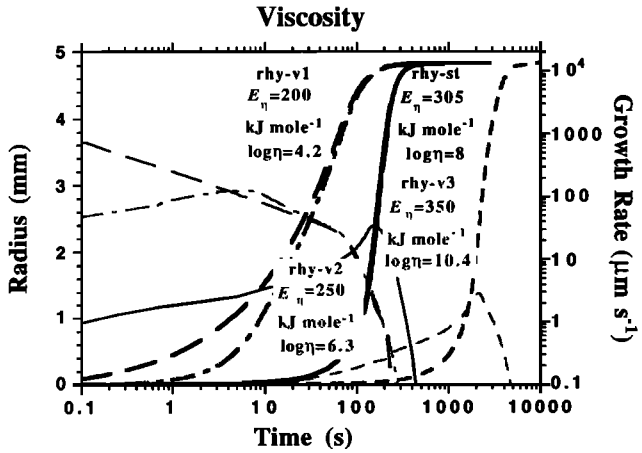

Figure 10. The effect of viscosity on bubble growth. Growth rate curves are shown as thin lines. The viscosity range spans values appropriate for dry melt compositions of andesitic basalt to super rhyolite. According to the model, viscosity is set by viscous flow activation energy E_η and is dependent on temperature and volatile concentration during degassing. Viscosity, in turn, affects diffusivity (equation (A33)). The complex interaction of viscosity with other system parameters makes it possible to include chemical composition of dry melt in the present model by specifying the appropriate E_η for the given composition.

will not affect viscosity. In the parametric study we used values for E_η of 200, 250, and 350 kJ mole^{-1} which can be taken to generally represent a range of melts from andesitic basalt to "super" rhyolite. Viscosity also depends on temperature and water concentration, both of which vary with time and space across the bubble wall during bubble growth such that the final viscosity can be 2 orders of magnitude greater than the initial viscosity (Table 4).

Variation of viscosity (E_η) in our numerical runs has a profound effect on the dynamics of bubble growth, causing variations in growth rate and time delay of several orders of magnitude. For example, with 1 wt% dissolved H_2O, andesitic basalt can degas in a few seconds at 1 bar, while it takes super rhyolite 2 hours (Table 4). The effect of viscosity on growth dynamics is illustrated in Figure 10. As was the case for temperature, the logarithmic slopes of the curves are similar with varying displacement along the time axis. The growth dynamics and viscosity relations can be found by regression such that

$$v_R,\ t_{delay},\ t_{final} \sim \eta^{0.825}\ (\text{Pa s}) \qquad (7)$$

It follows from (7) that bubble growth is quasi-proportional to viscosity and thus to initial activation energy as well as evolving temperature and dissolved volatile content throughout degassing.

3.7. Diffusivity

Diffusivity is a function of water concentration and temperature (equation A33). The initial value of diffusivity is defined by activation energy E_D and a free coefficient b (equation (A33) and Table 1). Fortunately, the value of b is nearly the same for rhyolitic and basaltic melts, and we assume that it is not significantly different for other dry melt compositions. Thus, in the parametric study we varied initial diffusivity only by activation energy. The results of the parametric study (Figure 11 and Table 4) indicate that growth rate has a logarithmic dependence on diffusivity, while the total growth time and initial time delay have a power law dependence such that

$$v_R \sim \log D$$
$$t_{delay} \sim D^{-0.3}$$
$$t_{final} \sim D^{-0.7} \qquad (8)$$

Numerical modeling allows examination of systems that may not be found in nature, thus providing some insights not otherwise evident. For instance a system with rhyolitic viscosity but which has high diffusivity appropriate for andesite will experience considerable dissipative (viscous) heating of the melt (up to 5.1 K) as a result of rapid bubble growth and melt displacement. The heating would be greater if initial water concentration and bubble number density were higher than in our standard rhyolite (see runs rhy-s1, rhy-c5, and rhy-d4 in Table 4). Note again that dissipative heating of the melt does not effect the final temperature of the system because it is balanced by bubble gas cooling (pdV work from the dynamic pressure term done on the viscous melt).

3.8. Summary of Interactive Parametric Study

In our parametric study the various magma parameters have been characterized in terms of their interactions with each other as well as with external conditions such as pressure and temperature. As such, the model is fundamentally different from previous models including *Proussevitch et al.* [1993] which did not account for any parametric interactions. The effects of variation of each parameter on bubble growth dynamics have been

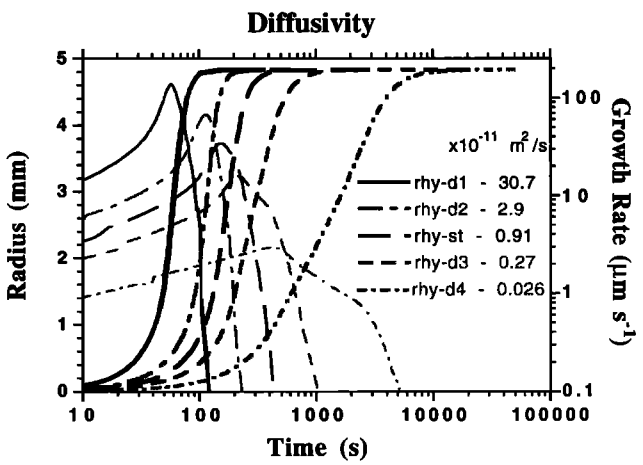

Figure 11. The effect of diffusivity on bubble growth in rhyolitic magma. Growth rate curves are shown as thin lines. Diffusivity is functionally related to viscosity, and, therefore, to temperature and volatile concentration. Parameter b (equation (A33)) was varied in numerical runs rhy-d1 to rhy-d4.

quantified and have elucidated the nature of the time delay, bubble overpressure, and other aspects of degassing which cannot be reliably assessed without a fully interactive model. Bubble growth rate, time delay, and total growth time are very sensitive to temperature, viscosity, diffusivity, and initial water concentration (oversaturation). We have found that ambient pressure does not significantly affect growth dynamics because expected sluggish growth at high pressures is counteracted by high diffusivity and water content. This is further explored in the decompressive study described below. In addition, bubble separation (number density) determines total growth time but has no effect on growth rate and time delay.

The effect of the interaction between parameters can be most clearly delineated by comparison with *Proussevitch et al.*'s [1993] previous noninteracting model. For instance, there is a marked contrast in the effects of initial water oversaturation and pressure. The interactive model also produces a more moderate dependence of bubble growth dynamics on these parameters. In addition, variable viscosity and diffusivity cause bubble growth rate to retard with time relative to the noninteracting case. This is because as volatiles exsolve, viscosity increases, diffusivity decreases, and the melt is capable of supporting higher volatile concentration gradients than it would if there were no parametric interaction. Another difference between the interactive and noninteractive model results is that the main phase of bubble growth (after the time delay) fits a logarithmic growth curve better than that for the noninteractive case. For application to actual volcanic systems it would be necessary to account for parametric interactions as well as system geometry, initial conditions, and flow dynamics. Toward this end, as a first step, we consider decompression of various hypothetical magmatic systems in section 3.

4. Decompressive Study With Constant Decompression Rate

In contrast to the parametric study, the decompressive model runs allow ambient pressure to decrease steadily to 1 bar from saturation pressure for a given dissolved volatile concentration. This simulates the decompression associated with the ascent of degassing magma. While this is critical aspect of degassing, it has not been neglected in previous models of magmatic bubble growth. *Proussevitch and Sahagian* 1996] recently addressed a simple case of this problem using a noninteractive, isothermal bubble growth model. It is thus now possible to compare the present results with the previous results, thereby isolating and quantifying the consequences of parametric interactions and thermal effects. In this way we may considerably extend our understanding of bubble growth and degassing processes which bear on the style and energetics of volcanic eruptions. While any variable decompression history can be specified in the model, we use various constant rates in this first demonstration of the model. Subsequently, when the model is applied to specific natural volcanic systems with observed or otherwise known conduit and magma reservoir geometries, the appropriate decompression histories can be used in the model as well.

We have restricted our decompressive numerical models to rhyolite melt compositions. We omit basalt because preliminary numerical runs (in addition to prior studies [*Proussevitch and Sahagian*, 1996]) have demonstrated that dynamic factors of bubble growth are relatively small in basaltic systems. This results from the low viscosity, high diffusivity, and thus low levels of oversaturation even for rapid rates of basaltic magma ascent [*Sparks et al.*, 1994]. Eruption models which assume gas-melt equilibrium at all times throughout magma ascent [*Dobran*, 1992; *Dobran and Coniglio*, 1996; *Wilson et al.*, 1980] are thus adequately suited to basaltic systems (although parametric interactions should still be included). Rhyolitic systems require more sophisticated models in which bubble growth dynamics include the evolving level of oversaturation as a function of ascent rate, time, position, and the various quantities addressed in the parametric model above. Of course, our simple model with constant decompression rates cannot be considered as a true simulation of energetic volcanic eruptions even if it does consider local gas-melt disequilibrium. However, the model can provide important constraints on dynamics, energetics, and mechanisms of energetic rhyolitic volcanic eruptions.

4.1. Conditions for the Decompressive Numerical Model

Rhyolitic melt transport properties such as viscosity, thermal and volatile diffusivities, and various magmatic parameters including initial temperature, density, heat capacity, water solubility law, surface tension, and initial bubble separation (number density) are taken from the parametric model (Tables 2 and 4). Initial bubble radius is set at 10^{-5} m to avoid issues of nucleation and long time delays for bubble growth. The initial volatile (water) concentration is calculated from the solubility law and bubble internal pressure such that the melt is saturated at the starting depth of magma rise.

Using these melt properties and bubble parameters, we conducted a series of model runs for magma initial depths of 1, 2, 3, 4, and 5 km. For each starting depth, nine runs were made with ascent rates of 0.01 - 100 m s^{-1}, making a total of 45 model runs for the rhyolitic system. In all cases the melt completed decompression and erupted while still oversaturated. The model subsequently continued computations, allowing the melt to degas at atmospheric pressure until exsolution was complete or oversaturated glass was produced.

The numerical model involves decompression rate because ambient pressure is an important parameter. However, in our discussion we will refer to the more easily visualized ascent rate commonly discussed in the literature. It is important to note that the decompression rate and ascent rate are not linearly related in a vesiculating magma because bulk magma density decreases with height in the column. Constant decompression rate implies an accelerating ascent rate. Even though "ascent rate" and "rise rate" are used in the following text and figures for convenience, the proper constant decompression rate was used in all model calculations. The values given for rise rate pertain only to ascent at the site of the conduit before vesiculation. We consider plug flow such that all points at

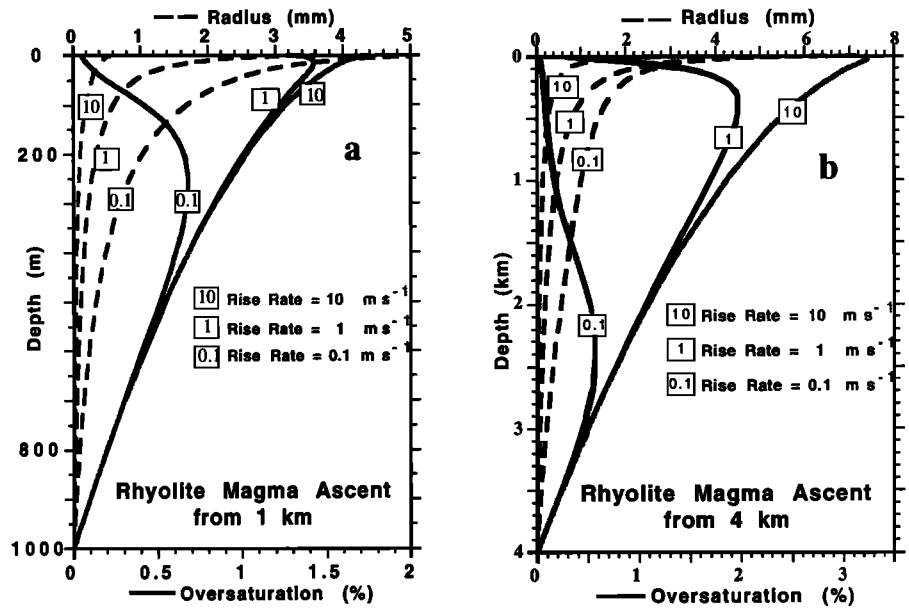

Figure 12. Results of decompressive model for bubble growth and H_2O oversaturation for ascending rhyolitic magma at constant decompression rate. Initial depths of magma ascent are (a) 1 km and (b) 4 km. The model assumes melt to be volatile-saturated at the initial depth (pressure). Very low initial ascent rates (0.01 and 0.1 m s^{-1} for starting depths of 1 and 4 km, respectively) can maintain quasi-equilibrium in the system throughout magma ascent. High ascent rates (10 m s^{-1} for starting depths of 1 and 4 km, respectively) can transport the rhyolite magma essentially undegassed to the vent, leading to rapid degassing and explosive expansion at the surface.

a given level in the magma have the same velocity and there is no deformation or viscous heating within the magma column.

In the model we do not consider bubble nucleation during decompressive rise because it depends on several factors which are determined by each volcanic system (e.g., liquid structure, number, shape, and composition of microlites) and the decompression history of each parcel of magma prior to eruption. Because of the complexity and individual nature of the factors which control nucleation, we do not quantitatively assess nucleation processes in the present model. However, some qualitative results do emerge related to volatile oversaturation history, and these can be assessed. Even without consideration of additional nucleation during bubble growth, our present model results may be volcanologically relevant because it has been suggested that in at least some cases, bubbles nucleate during a short time interval at an early stage of decompression with little subsequent nucleation [*Toramaru*, 1989, 1995]. In subsequent studies we will explore the complexities introduced by additional nucleation during mid-stage to late-stage bubble growth.

4.2. Magma Ascent Within the Conduit

The effect of magma ascent within the conduit can be characterized in terms of volatile oversaturation, bubble radius, melt temperature, and other parameters as a function of depth for various decompression rates. Water oversaturation for rising magma with starting depths of 1 and 4 km is illustrated in Figure 12. The character of degassing depends on the rate of magma ascent.

4.2.1. Low ascent rates. We consider a melt which is oversaturated with water <0.1 wt% to be in quasi-equilibrium with ambient pressure. For rhyolite with geologically reasonable characteristics, quasi-equilibrium can be maintained when ascent rates are <0.01 m s^{-1} for a starting depth of 1 km, and <0.05 m s^{-1} for a starting depth of 4 km.

4.2.2. Intermediate ascent rates. At ascent rates between 0.1 and a few m s^{-1}, magmas starting from 1 km have an oversaturation maximum midway up the conduit, approaching equilibrium toward the surface. The position of maximum oversaturation rises as the ascent rate increases. In contrast, magmas ascending at 1 m s^{-1} from 4 km maintain a relatively constant level of oversaturation (Figure 12b). We attribute this to the evolving saturation concentration of water which affects diffusivity and viscosity.

4.2.3. High ascent rates. Degassing behavior at high ascent rates of rhyolite magma is indicated by curves 1 and 10 on Figure 12. At high rates of magma ascent, diffusivity of dissolved gas into bubbles cannot keep pace with the rates of decompression and associated solubility decrease. This leads to increasing volatile oversaturation during magma ascent. Nevertheless, there can be an oversaturation maximum very close to the surface (uppermost 10-30 m) (see curves 1 and 10 in Figures 12a and 12b, respectively).

These three magma ascent and degassing regimes bear on eruption styles of rhyolitic volcanism because they effect bubble growth dynamics, magma volumetric expansion, and disruption of foam into spray and pyroclasts near or at the surface. We have attempted to

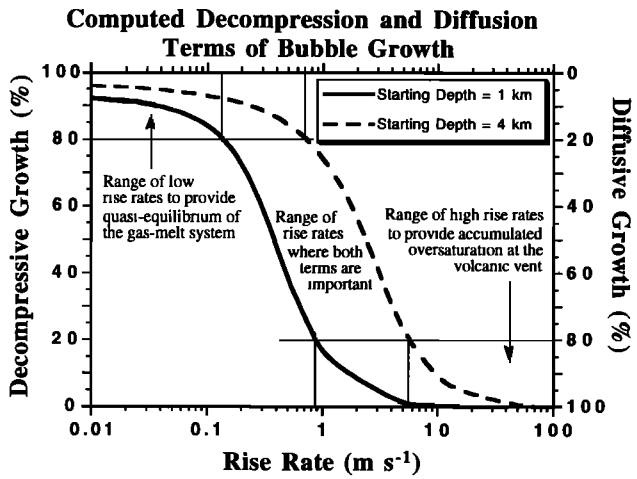

Figure 13. Decompressive and diffusive contributions to bubble growth in our standard magma (Tables 2 and 4) for magma ascent from 1 and 4 km. The contributions have been computed and integrated for initial ascent rates of 0.01 to 100 m s^{-1} and interpolated to create these curves.

qualitatively assess the styles of degassing on the basis of these three regimes. Toward this end, we separated diffusive and decompressive contributions to bubble growth at each time step in the model and integrated them over the time of bubble growth (Figure 13). The decompressive contribution included an additional bubble growth term due to volatile influx in response to the decrease in volatile solubility with decompression (assuming no diffusivity limitations). As the magma reaches the surface some dynamic overpressure still exists [*Proussevitch et al.*, 1993], but this is quickly relieved at the surface, and the decompression term goes to zero. Subsequent degassing at the surface is driven solely by the diffusive term. Thus, in general terms, faster decompression leads to degassing primarily by the diffusion term because the essentially undegassed magma erupts to 1 atm and exsolves without further decompression. Conversely, slow decompression maintains gas-melt equilibrium, and the decompression term accounts for all degassing. Ascent rate regimes can thus be separated on the basis of the relative contributions of decompression and diffusion to bubble growth (Figure 13). The transition from a slow to an intermediate ascent rate occurs when the diffusive contribution reaches 20% of the total, and the transition to a high ascent rate occurs at 80% diffusive contribution. For magmas starting at 1 km, transitional ascent rates are ~0.1 and 1.0 m s^{-1}, respectively, and for 4 km they are 0.7 and 6 m s^{-1}.

4.3. Volatile Oversaturation at the Vent

The character and energetics of eruption depends strongly on the level of oversaturation of magma as it reaches the vent [*Johnson et al.*, 1994]. Figure 14 reveals that oversaturation at the vent is independent of initial depth of magma ascent for initial depths of >2 km. This results from the effects on bubble growth dynamics of the indirect pressure dependence of diffusion (via concentration) and the physical effect of thinner bubble walls at shallow depths in deeper-derived systems. It is fortuitous that the various interactions conspire to approximately eliminate magma starting depth as an important control on surface oversaturation levels. This makes it possible to draw a single curve which includes the overlapping individual curves in Figure 14 for a representation of surface oversaturation (Figure 15). This could not have been predicted without the detailed interactive model and leads to important applications. It should be noted that at sufficiently high ascent rates, there is no degassing, and erupted material contains all of the initially dissolved volatiles (Figure 14).

Because the relative contribution of decompressive and diffusive bubble growth affects eruption style, it is important to be able to account for the changes in the oversaturation of magmas en route to the surface. With rapid ascent, diffusion rates are insufficient to maintain equilibrium, resulting in eruption of highly oversaturated magma. Subsequent diffusive bubble growth at 1 bar in the eruption column can be explosive and thus bears on volcanic hazards. Our model results indicate that the extent of oversaturation at the vent depends on the ascent (decompression) rate rather than initial depth (Figures 14 and 15). Consequently, for magmas from depths of more than 2 km the model results can be inverted and used as a tool for the determination of ascent rates on the basis of observed quenched glasses which record the oversaturation of erupting melt [*Anderson et al.*, 1989; *Dunbar and Kyle*, 1992; *Eichelberger and Westrich*, 1981; *Melson et al.*, 1990; *Newman et al.*, 1986]. We can derive a set of empirical relations on the basis of logarithmic and power regressions of surface oversaturation (Figure 15) for various starting depths as follows:

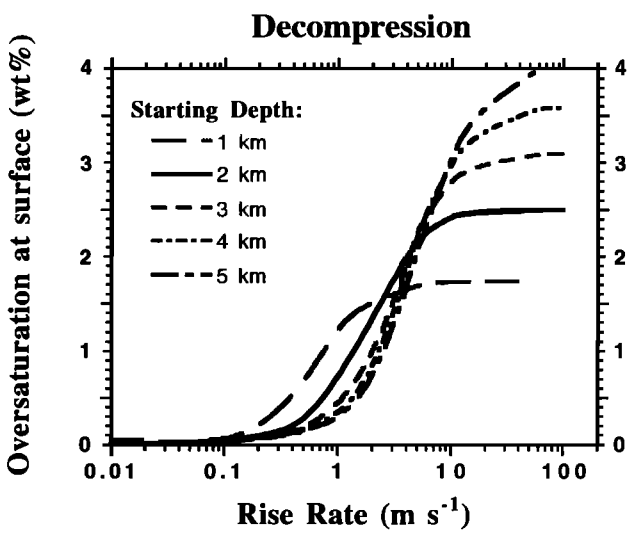

Figure 14. Oversaturation of standard rhyolitic melt at the vent as a function of ascent rate for various initial magma depths. An unexpected result of the model is that oversaturation at the vent does not depend on the initial depth. This result can be used for reconstruction of magma withdrawal dynamics by analysis of quenched obsidian glasses. The overlap of the various curves can be explained on the basis of interactions between competing parameters and total bubble volume fraction which makes thinner bubble walls (smaller diffusion distance) for deep-derived magmas when they reach shallow depths.

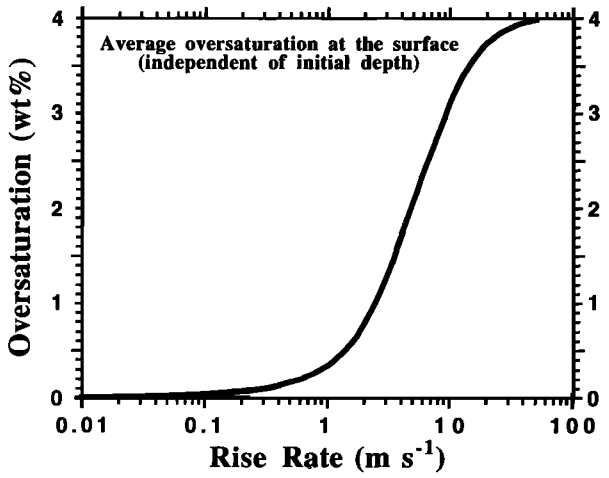

Figure 15. Oversaturation of standard rhyolitic melt at the vent averaged over all initial depths (see Figure 14, equations (9a) and (9b)). This curve can be used to estimate magma decompression rate from analyses of water oversaturation in glassy eruption products.

$$v_{rise}\,(\mathrm{m\ s^{-1}}) = 0.31\,x^{0.94}\,(\mathrm{wt\%\ H_2O}) \qquad r = 0.9997 \quad x < 0.5\ \mathrm{wt\%\ H_2O} \tag{9a}$$

$$v_{rise}\,(\mathrm{m\ s^{-1}}) = 0.27 + 2.8 \log x\,(\mathrm{wt\%\ H_2O}) \qquad r = 0.9968 \quad x \geq 0.5\ \mathrm{wt\%\ H_2O} \tag{9b}$$

For rhyolites with properties similar to those specified in Table 2 it is possible to use (9a) and (9b) to estimate magma ascent rates if water content in quenched glass can be measured. For most hydrous obsidians with 2-4 wt% H_2O, ascent rates would be tens to hundreds of m s^{-1}, assuming the ability of the magma to nucleate bubbles. Without nucleation, high volatile oversaturation would be observed even for low ascent rates. Maximum oversaturation occurs below the surface for low and intermediate ascent rates, as illustrated in Figure 16.

If nucleation were to be included in the model, the depth of maximum oversaturation would have special significance. While nucleation may occur below this depth, depending on local oversaturation (and various other factors), the maximum nucleation rate would be expected to occur at the depth of maximum oversaturation. This depth would be greater if there was nucleation of additional bubble between existing bubbles, causing diffusion distances to be less. However, because oversaturation decreases above this point, we would not expect any subsequent nucleation. This has been suggested independently by *Toramaru* [1995]. Consequently, the important late-stage bubble growth processes should not be affected by nucleation, and omission of nucleation in our decompressive model would not introduce any quantitative errors in the rapid bubble growth which occurs near and at the vent.

4.4. Temperature in Decompressive Model Runs

Temperature variations during magma ascent and eruption affect rheology, fluid dynamics, and ultimately, vitrification and foam fragmentation (fluid or brittle). We consider an adiabatic system and include the thermal effects of volatile (water) vaporization, work of gas expansion (pdV), dissipative heating, and redistribution of the heat within the system (thermal diffusivity). Crystallization and vitrification provide heat to the system according to (B8).

We can consider the thermal effects separately for magma degassing within the conduit and at the surface. Temperature variations within the conduit caused by heat of vaporization and pdV work for various ascent rates are illustrated in Figure 17. Three aspects of thermal behavior emerge from the decompression model.

1. Temperature decreases in the upper section of the conduit as the melt approaches the vent. Shallower initial depth of magma ascent leads to steeper parabolic curves of total temperature. Temperature does not follow bubble radius (compare Figure 17 with Figure 12) indicating a non-linear relation between temperature change and volatile exsolution.

2. Temperature of magma within the conduit is very sensitive to magma ascent rate. The lowest temperature profiles are for low ascent and decompression rates with quasi-equilibrium degassing (0.1 on Figure 17). At the other extreme, high ascent rates lead to no significant temperature change within the conduit (1 and 10 on Figure 17a and 17b respectively) because magma is delivered to the surface so quickly that no significant degassing can occur in the conduit.

3. Heat of vaporization and pdV work are comparable at depths >~2 km (see Figure 17b). Cooling due to vaporization increases during decompression because it is highly pressure dependent (greater at low pressures), but pdV work is relatively insensitive to pressure [*Sahagian and Proussevitch*, 1996] so that at shallow depths, vaporization cooling dominates the thermal behavior of the system.

There can also be significant temperature change after the magma reaches the surface. Figure 18 shows melt

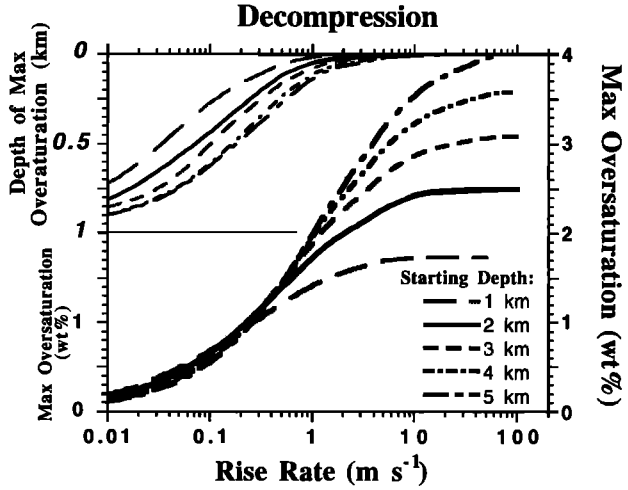

Figure 16. Maximum oversaturation of standard rhyolite melt and dimensionless depth of maximum oversaturation both depend on magma ascent rate and initial depth of magma ascent. For low ascent rates the depth of maximum oversaturation is in the lower part of the conduit, but for rapid ascent rates it moves up to vent (see Figure 14).

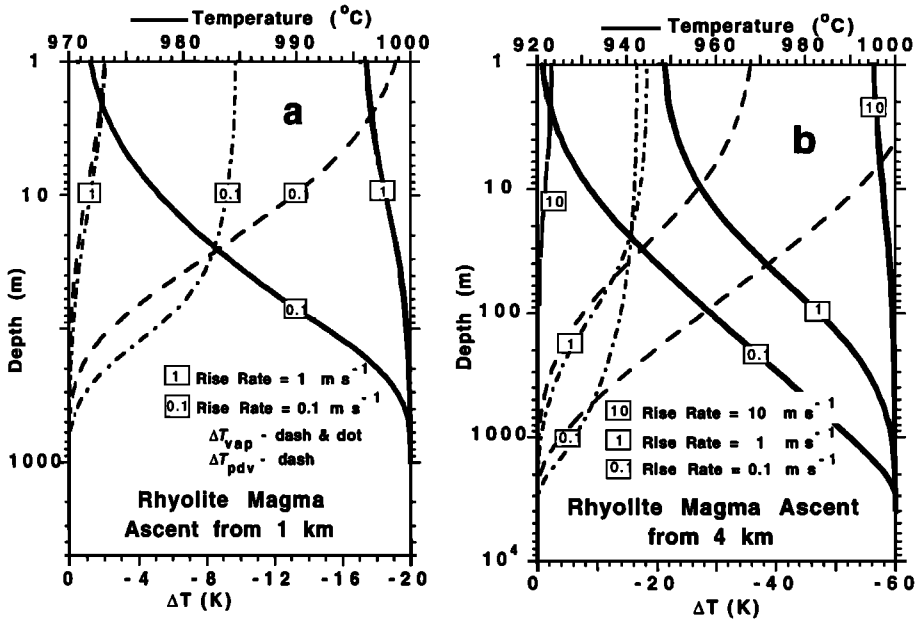

Figure 17. Thermal results of decompressive model for adiabatic ascent of rhyolitic magma at various constant decompression rates. Initial depths of magma ascent are (a) 1 and (b) 4 km. Solid curves show total temperature of the system. Dot-dashed curves are the exsolution cooling term, and dashed curves are the pdV cooling term. Considerable cooling occurs as the magma approaches the vent. At a given depth, a lower ascent rate leads to a lower magma temperature. If magma is rapidly transported to the vent without significant degassing, no temperature change is observed until degassing commences at the vent. Vaporization cooling dominates at shallow depths, but vaporization and pdV contributions are comparable at depth.

temperature as the magma reaches the vent as well as final temperature when degassing is completed. For very low ascent rates, surface and final temperatures are similar because no additional degassing occurs at the surface. As ascent rates increase, this difference increases because a greater portion of total degassing occurs at the surface. Final temperature is greater for faster ascent rates because the magma is farther from equilibrium when it reaches the surface so that cooling is only due to heat of vaporization. (Expansion due to vaporization does essentially no cooling.) Slow ascent maintains equilibrium so that cooling is due to both vaporization and gas expansion (equations (19) and (20)) [*Sahagian and Proussevitch*, 1996]. Note that for some cases of magma ascent (high initial depth), temperature drops almost to vitrification temperature (Figure 18). If the initial saturation depth is >5 km, then adiabatic decompression and degassing could cause crystallization before reaching the surface [*Harris*, 1977], but at such great depths, CO_2 is also present which significantly reduces total volatile solubility [*Mysen*, 1977; *Stolper and Holloway*, 1988].

Cooling at the vent bears on the processes of foam disruption into ash and other pyroclastic material. If temperatures approach the vitrification point, then brittle fragmentation into angular pyroclasts may occur instead of disruption into liquid spray [*Alidibirov*, 1994; *Wohletz et al.*, 1989]. Even if gas leaves the foam through interpore channels without bursting it into fragments [*Cashman and Mangan*, 1994], vaporization cooling of the melt can lead to adiabatic vitrification without the necessity for radiative cooling to the atmosphere.

4.5. Decompression Regimes and Explosive Eruptions

An assessment of the response of eruption style to ascent rate suggests that the evolution of oversaturation, bubble radius, gas fraction, etc., during magma rise sets the stage for eruption processes at the vent (Figures 12-17). Decompressive and diffusive expansion are the two main factors that control eruption style and are the cause of special concern because of potential volcanic hazards.

1. Decompressive growth is expansion of a bubble due to decompression. It consists of two terms: (1) expansion of previously exsolved gas and (2) exsolution due to reduced solubility in response to decompression. The former does not depend on decompression rate, while the latter applies only to equilibrium degassing (slow decompression) [*Proussevitch and Sahagian*, 1996; *Sahagian and Proussevitch*, 1996].

2. Diffusive growth is expansion of the system due to diffusion of oversaturated volatiles into the bubbles at constant pressure. Degassing and bubble growth dynamics at constant pressure depend strongly on volatile oversaturation (Figure 7). Magma ascent rates play a key role in water oversaturation at the surface (Figure 15). It is thus necessary to define a range of decompression rates for which the oversaturation factor is important and to compare it with the decompressive factor.

4.6. Eruptions

We extended the simple model geometry of the bubble elementary cell to the scale of a volcanic system to explore

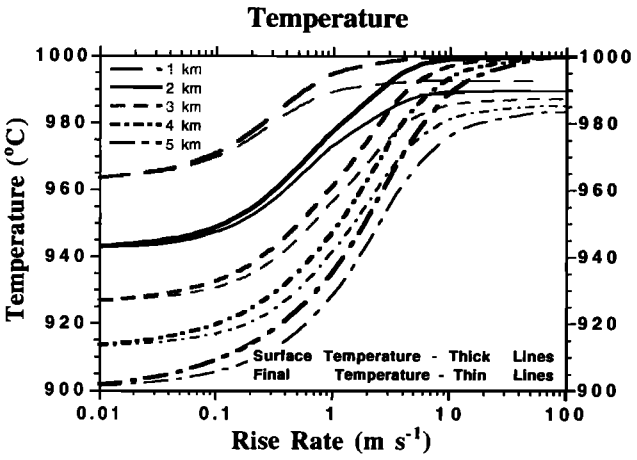

Figure 18. Temperature at the vent (when magma reaches the surface) and final temperature (when degassing is completed) for various ascent rates and starting depths. Surface temperatures approach an initial magma temperature of 1000°C (Table 3) as ascent rate approaches 10 m s^{-1}.

the large-scale effects of degassing processes. As an example, we have chosen a 300 m radius for a cylindrical volcanic conduit as a representative for silicic volcanoes based on field estimates for various documented eruptions [*Carey and Sigurdsson*, 1987; *Gardner et al.*, 1991; *Wilson*, 1980].

The rate of magma expansion at the vent can be considered as ash cloud front velocity. After reaching the vent we take the eruption cloud to form a hemisphere centered on the vent which expands according to addition of volume of eruptive products from the vent. Once gas fraction exceeds the disruption threshold in the vent, the numerical model computes diffusive degassing until the system reaches equilibrium at atmospheric pressure (Figure 19). The geometry of the conduit is not fixed a priori. However, it is constrained by the condition of constant rate of decompression at every point in the magma column. The constant rate of decompression implies upward acceleration for a cylindrical conduit. This is a result of the decrease in density caused by vesiculation at higher levels.

For shallow magma chambers (Figure 19a), expansion velocity of 60-90 m s^{-1} can result if magma ascent rate is greater than 1 m s^{-1}. This maximum velocity does not depend on the initial ascent rate because essentially undegassed magma expands at 1 bar diffusive bubble growth in any case. For low ascent rates (0.1 m s^{-1}), the gas-melt system maintains quasi-equilibrium during ascent. There is a very marked difference in the character of eruption between 0.1 and 1 m s^{-1}. The front velocity spike at zero time (when magma reaches the vent) for an ascent rate of 1 m s^{-1} indicates that decompression provides an important contribution to system expansion at this ascent rate. Maximum front velocities which occur after reaching the vent indicate an increase of the diffusive degassing factor in system expansion and a decrease of decompression factor (see thin lines on Figure 19).

If the initial depth of magma ascent is >3 km, the maximum ash cloud velocity becomes supersonic (for a conduit radius of 300 m). For greater initial depths the decompression factor is important for magma ascent rate of ~10 m s^{-1}, but is minor for higher ascent rates where diffusive degassing dominates. With slow rates of ascent, explosive eruptions do not occur even when the magma starts at great depths (Figure 19).

Maximum front velocity and the duration of explosive eruption are related. Higher front velocity leads to a narrower peak (Figure 19). This is because the energy of eruption is closely related to initial volatile content in the system and thus to the cube of final bubble radius. Thus the energy of eruption is proportional to the area under each curve in Figure 19. Modeled variation of the starting depth from 1 to 4 km increases the initial saturation water content and therefore the energetics of the system by a factor of 2 (1.86 and 3.72 wt% H_2O, respectively) but this is much less than the difference in maximum front velocities (factor of 10).

Note that the ash cloud front velocity is proportional to the conduit radius because the lateral velocity of the cloud edge is determined by the cumulative expansion of every bubble within the cloud. Observations and estimates of ejecta velocities range from 350 m s^{-1} for 1980 Mount St. Helens [*Carey et al.*, 1990] and 79 A.D. Vesuvius eruption [*Carey and Sigurdsson*, 1987] to 600 m s^{-1} for the Bishop Tuff eruption [*Gardner et al.*, 1991] at 1 kbar and 10 m s^{-1} [*Anderson*, 1991] respectively. The decompression model is consistent with these numbers (Figure 19d), but it will be necessary to develop a more complex model to account for the feedback between interacting bubble growth dynamics, ascent rate, and conduit geometry in order to relax the unrealistic constraint of constant magma decompression rate.

5. Conclusions

1. Models which do not account for variations and interactions of parameters during bubble growth cannot effectively simulate natural eruptions. The widely cited parabolic law for bubble growth ($R \sim t^{1/2}$) is not valid for most magma degassing conditions with or without interaction with neighboring bubbles. It is appropriate only for slow degassing with small oversaturation at high and constant ambient pressure. Our results indicate that a logarithmic relation $R \sim \log(t)$ is more appropriate for the active period of bubble growth, but even this does not apply for many cases.

2. The time delay for bubble growth results from two independent sources. The first is the initial bubble size which causes time delay to increase as the initial model radius approaches the nuclear radius from above (equation (3)). This is because surface tensions pressure in the bubble reduces the effective oversaturation of volatiles at the bubble interface, thus reducing the adjacent concentration gradient. The second is a dynamic factor which depends on volatile oversaturation and other melt properties (viscosity, diffusivity, etc.). The time delay is related to the total duration of bubble growth, and for rhyolite melts at low pressures it represents ~10 % of the total bubble growth time.

3. The most important parameters that control the dynamics of bubble growth are interacting (1) viscosity,

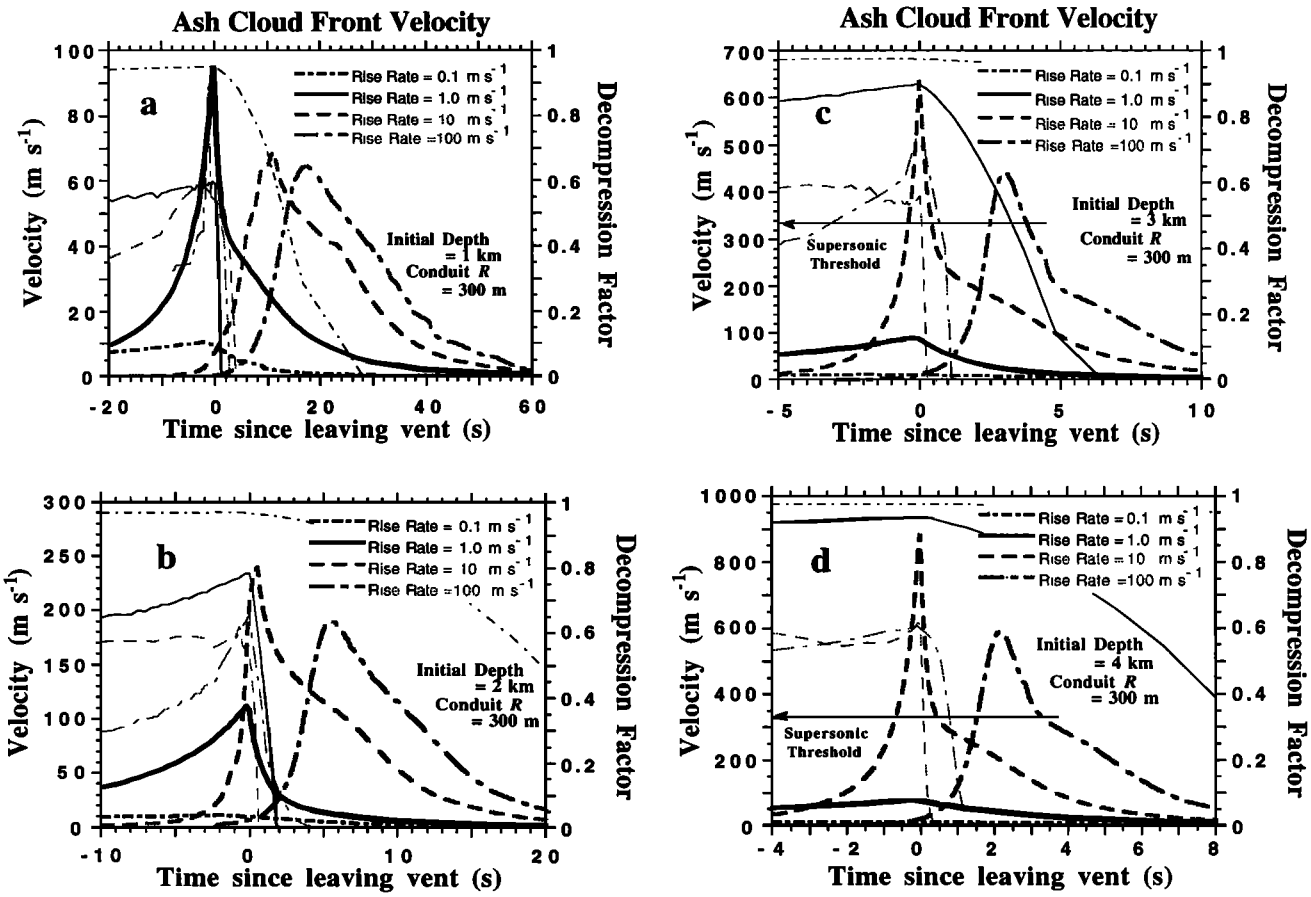

Figure 19. Modeled bubble growth dynamics for a typical volcanic system. Expansion of the system at the vent and beyond is displayed here as ash cloud front velocity because it is assumed that magma at this point passes the fragmentation threshold of 80-90 gas volume percent. The results are given for cases with starting depths of (a) 1, (b) 2, (c) 3, and (d) 4 km. According to model rescaling, ash cloud velocity is proportional to the initial conduit radius (we use 300 m). The decompression factor reflects the relative contributions of diffusive and decompressive bubble growth and is shown as thin lines. Explosive eruption is unlikely for shallow-derived magmas (<1 km), but for deeper-derived magmas, explosive eruptions are possible for sufficiently high ascent rates.

(2) diffusivity, (3) temperature, (4) ambient pressure, (5) volatile (H_2O) concentration, and (6) bubble separation. Each of these six parameters and their interactions can change total bubble growth time by 2-4 orders of magnitude. These important interactions have never before been considered in magmatic degassing models. The interactions make for a more moderate dependence on initial oversaturation and pressure than noninteractive models. The parametric study revealed the sensitivity of the system to the various parameters and revealed some nonintuitive results, for example, that it can take more time to degas a magma with a lower initial dissolved volatile content than one with a higher volatile content (due to thinner walls and shorter diffusion distances).

4. The decompression model for bubble growth, degassing, and foam expansion with constant decompression rate indicates that magma ascent rate is of primary importance in controlling eruption dynamics. The starting depth of magma ascent plays a less significant role. The most intensive degassing and expansion of bubbly magma occurs at the vent regardless of ascent rate or initial depth.

5. Water oversaturation during magma ascent is very sensitive to ascent rates (equation (5)). Low ascent rates (<0.1 m s^{-1}) allow the maintenance of quasi-equilibrium (very low oversaturation). Higher ascent rates produce constant or linearly increasing oversaturation with decompression. With rapid ascent rates (>10 m s^{-1}), the magma does not have sufficient time available to degas significantly, and magma is delivered to the surface with essentially the same concentration of volatiles that it started with at depth. In this case almost all degassing and magma expansion takes place at the surface at constant ambient (atmospheric) pressure. This limiting case approaches the condition of instantaneous degassing of the parametric model.

6. Initial magma depth does not affect volatile oversaturation at the vent (Figures 13-15). This result could be used in conjunction with field campaigns in subsequent reconstructions of magma dynamics of historical and observed eruptions on the basis of volatile concentrations in quenched undegassed obsidians.

7. Temperature variations during magma ascent are significant only at the vent where cooling due to water

vaporization is the most important factor. At high pressures, vaporization and pdV work are comparable cooling terms. The total net cooling of rhyolitic melt can lead to vitrification if the ascent rate is greater than a few m s^{-1}, and thus can contribute to brittle foam fragmentation into fine ash.

8. Energetic explosions are likely to occur only for magma originating from relatively deep chambers (>3 km). Ash cloud front velocity increases abruptly with magma ascent rate with an important transition to explosive behavior at ~3-10 m s^{-1} depending on initial depth. Additional ascent rate increase does not further increase explosion velocities significantly. Ash cloud front velocity is also dependent on conduit radius. For a radius of 300 m the front velocity becomes supersonic for a 3 km initial magma depth.

9. The relative contributions of decompressive and diffusive factors of bubble growth depend on prior bubble growth history and magma ascent rate. For slow ascent rates (<0.1-1 m s^{-1}) decompressive bubble growth dominates with little or no oversaturation at the vent and produces gentle effusive eruptions. For higher ascent rates, diffusion and decompression are both important and can lead to explosions with a sharp peak of expansion velocity at the time when magma reaches the vent. With rapid magma ascent (>10-20 m s^{-1}), there is negligible decompressive bubble growth during ascent (because volatiles are still in solution and not in bubbles), but diffusive bubble growth causes explosive expansion within a few seconds of reaching the vent. In the case of basalts, diffusion rates are sufficiently rapid to keep the system near chemical equilibrium such that oversaturation is small or negligible and bubble growth is solely decompressive.

10. Oversaturation of erupting magma at the vent does not depend significantly on initial depth but rather on decompression rate (ascent rate). It should thus be possible under certain conditions to invert our model results to determine the ascent rate from oversaturation observed in quenched volcanic glasses.

11. Our numerical model provides a tool for increased understanding of the processes which drive volcanic eruptions. The parametric study allowed quantification of the sensitivity of the modeled system to variations in each of the magmatic properties and physical conditions for a variety of geologically reasonable scenarios. The greatest utility of simple (although usually unrealistic) models is in isolating the influence of each parameter and determining which parameters must be well constrained (experimentally or otherwise) in future attempts to describe natural systems. A model such as the one presented in this paper should never be confused with a simulation which is a descriptive tool. Our model is used to diagnose the system. The purpose of a simulation is to mimic a natural system without concern about driving forces or system sensitivities. We do not yet try to mimic a natural system and thus do not try to compare our model results to natural eruption products. Any resemblance would be coincidental as there are some eruption processes not included in our model which would affect the vesicularity and dissolved volatile contents of eruption products. We hope that the deeper understanding of the processes and sensitivities of magmatic systems provided by our model results will ultimately lead to the ability to make a more realistic simulation of observed volcanic systems.

12. The numerical models (FORTRAN codes) presented in this paper are freely available from the authors.

Appendix A: Analytical Formulation

A1. Continuity and Momentum

The continuity equation specifies mass conservation during fluid flow as

$$\frac{\rho}{\partial t} + \mathrm{div}\,\mathbf{j} = 0 \tag{A1}$$

For equation notations and a list of variables used throughout this discussion, see Table A1. In spherical coordinates with appropriate boundary conditions the continuity equation becomes

$$v_r = v_R R^2 \frac{1}{r^2} \tag{A2}$$

The momentum equation specifies the forces affecting movement of the liquid and is generally written as

$$\rho \frac{Dv}{Dt} = -\,\mathrm{grad}\,p + \partial_K \tau_{iK} \tag{A3}$$

where D/Dt is the substantial derivative. For spherical coordinates, (A3) transforms to

$$\rho\left(\frac{\partial v_r}{\partial t} + v_r \frac{\partial v_r}{\partial r}\right) = -\frac{\partial p}{\partial r} + \frac{1}{r^2}\frac{\partial}{\partial r}\left(r^2 \tau_{rr}\right) - \frac{\tau_{\theta\theta} + \tau_{\varphi\varphi}}{r} \tag{A4}$$

With spherical symmetry, $\tau_{\theta\theta} = \tau_{\varphi\varphi}$, and (A4) can be rewritten as

$$\rho\left(\frac{\partial v_r}{\partial t} + v_r \frac{\partial v_r}{\partial r}\right) = -\frac{\partial p}{\partial r} + \frac{\partial \tau_{rr}}{\partial r} + 2\left(\frac{\tau_{rr} - \tau_{\theta\theta}}{r}\right) \tag{A5}$$

In this case the stress tensor for a Newtonian incompressible liquid is [*Landau and Lifshitz*, 1987]

$$\tau_{rr} = -p + 2\eta \frac{\partial v_r}{\partial r} \tag{A6a}$$

$$\tau_{\theta\theta} = \tau_{\varphi\varphi} = -p + 2\eta \frac{v_r}{r} \tag{A6b}$$

Boundary conditions for (A5) appropriate for bubble growth (Figure 1) are

$$p(R) - \tau_{rr}(R) = p_g - \frac{2\sigma}{R} \tag{A7a}$$

$$p(S) - \tau_{rr}(S) = p_f \tag{A7b}$$

Integration of (A5) over the r coordinate within the fluid shell between R and S, and application of the boundary conditions and the continuity equation (A2) yields

Table A1. Notation List

Symbol	Description	Unit	Eqation
b	diffusivity constant	None	(A32)
B	universal gas constant	J K^{-1} $mole^{-1}$	(A12)
c	heat capacity	J K^{-1} kg^{-1}	(A18)
D	chemical diffusivity coefficient	m^2 s^{-1}	(A12)
E	energy of activation	J $mole^{-1}$	(A28)
H	enthalpy	J	(A17)
j	mass flux	kg $m^{-2}s^{-1}$	(A1)
J	heat flux	J $m^{-2}s^{-1}$	(A16)
k_η	viscosity constant	None	(A30)
k_w	henry's analog constant	None	(A35)
K_h	solubility constant	Pa^{-1}	(A15c)
Le	lewis number	None	(B11f)
m	mass	kg	(A11)
M	molecular weight of a volatile gas	kg $mole^{-1}$	(A12)
p	pressure	Pa	(A3)
Q	heat	J kg^{-1}	(A23)
r	radial direction of spherical coordinate system	m	(A2)
R	radius of a gas bubble	m	(A2)
s	surface area	m^2	(A11)
S	bubble cell border radius	m	(A7b)
t	time	s	(A1)
T	temperature	K	(A12)
v	radial velocity	m s^{-1}	(A2)
V	volume	m^3	(A16)
W	temperature diffusivity potential function	m^3	(B2b)
x	concentration fraction of a volatile in a melt	None	(A12)
X	concentration of a chemical component	kg m^{-3}	(A13)
y	lagrangian coordinate variable	m^3	(B1)
z	parameter $z = 1/r^3$	m^{-3}	(A8)
χ	temperature diffusivity	m^2 s^{-1}	(A21)
Φ	volatile diffusivity potential function	m^3	(B2a)
κ	heat conductivity	J m^{-1} s^{-1}	(A26)
η	dynamic viscosity	Pa s	(A6)
π	constant	None	(A18)
ρ	density of the melt	kg m^{-3}	(A1)
σ	surface tension	N m^{-1}	(A7a)
τ	stress tensor	Pa	(A3)
ν	kinematic viscosity	m^2 s^{-1}	(A26)
	Subscripts		
0	parameter at the initial time		
con	conductivity term of heat transfer		
D	diffusivity related parameter		
ev	vaporization term (cooling)		
ex	expansion term (pdV cooling)		
g	parameter inside the gas bubble		
f	ambient parameter (pressure)		
i	components of three-dimensional coordinate systems		
K	components of three-dimensional coordinate systems		
m	melt parameter		
p	pressure parameter		
R	parameter at the surface of gas bubble		
r	radial component of vector in spherical coordinate system		
S	parameter at the outer border of bubble cell		
v	dynamic parameter (pressure)		
vt	vitrification parameter (heating)		
μ	chemical potential		
θ	colongitude of vector in spherical coordinate system		
ϕ	colatitude of vector in spherical coordinate system		
η	viscosity parameter (energy of activation)		
σ	surface tension parameter (pressure)		

Bold font is used for vector parameters, and a circumflex is used for dimensionless parameters.

$$p_g - p_f = \frac{2\sigma}{R} - 4 v_R R^2 \int_{z(R)}^{z(S)} \eta(z)\, dz + \rho R \frac{dv_R}{dt}\left(1 - \frac{R}{S}\right) + \rho v_R^2 \left(\frac{3}{2} - 2\frac{R}{S} + \frac{1}{2}\frac{R^4}{S^4}\right) \quad \text{(A8)}$$

where $z = 1/r^3$. The two rightmost terms of (A8) are inertial terms which are commonly neglected. For viscous fluids such as magmatic melts, inertial terms are 5 - 15 orders of magnitude smaller than the next smallest pressure term in (A8).

Combining the equations for continuity and momentum, we obtain

$$p_g - p_f = \frac{2\sigma}{R} - 4 v_R R^2 \int_{z(R)}^{z(S)} \eta(z)\, dz \quad \text{(A9)}$$

for the case of variable viscosity. If the viscosity were constant, then (A9) would reduce to the simpler form used by *Proussevitch et al.* [1993, equation 7]. Bubble pressure p_g consists of three components such that

$$p_g = p_f + p_\sigma + p_v \quad \text{(A10)}$$

where p_f is ambient pressure, p_σ is surface tension pressure, and p_v is dynamic pressure.

A2. Mass Balance and Diffusion

Diffusion of volatiles into the bubble from oversaturated melt is the primary driving mechanism of bubble growth. To meet the requirements of volatile mass conservation in the system, volatile mass flux at the bubble interface must be balanced against volatile species diffusion in the surrounding melt. At the bubble interface,

$$\frac{dm}{dt} = s\,\mathbf{j} \quad \text{(A11)}$$

where s is the surface area of the bubble. The behavior of gas within the bubble can be approximated by the ideal gas law which is valid for water at magmatic temperatures and pressures [*Weast*, 1976]. We can thus rewrite (A11) as

$$d\left(\frac{P_g R^3}{T_g}\right) = 3\frac{B}{M} R^2 D \rho \left(\frac{\partial x}{\partial r}\right)_{r=R} dt \quad \text{(A12)}$$

which represents the bubble growth rate as a function of volatile concentration gradient at the bubble interface. Equation (A12) differs from (9) given by *Proussevitch et al.* [1993] in that it includes a temperature term.

Consider now the diffusion of volatiles in the melt. The diffusion equation can be written generally as

$$\frac{DX}{Dt} = -\,\mathrm{div}\,(D\,\mathrm{grad}\,X) \quad \text{(A13)}$$

where D on the left-hand side is the material derivative (not be confused with the common notation for diffusivity used on right-hand side) and X is concentration (kg m^{-3}).

In spherical coordinates with spatially variable concentration and diffusivity, (A13) becomes

$$\frac{\partial x}{\partial t} + v_r \frac{\partial x}{\partial r} = \frac{1}{r^2}\frac{\partial}{\partial r}\left(D r^2 \frac{\partial x}{\partial r}\right) \quad \text{(A14)}$$

where x is mass fraction. Initial and boundary conditions for (A14) are

$$x(r,0) = x_0 \quad r > R \quad t = 0 \quad \text{(A15a)}$$

$$\left(\frac{\partial x}{\partial r}\right)_{r=S} = 0 \quad t > 0 \quad \text{(A15b)}$$

$$x(R,t) = x_R = \left(K_h p_g\right)^{1/n} \quad r = R \quad t > 0 \quad \text{(A15c)}$$

In (A15a) we specify a uniform initial concentration, although it is possible to specify any initial concentration distribution. Equation (A15b) indicates that there is no volatile flux through the outer surface of the elementary cell. Equation (A15c) relates to (A14) and sets the volatile concentration at the bubble interface to be in equilibrium with gas pressure within the bubble. This is expressed by Henry's law in which n = 2 for water up to a few hundred MPa [*Burnham*, 1975; *Sparks*, 1978; *Toramaru*, 1995].

Equations (A14) and (A15) define the volatile concentration profile across the bubble wall. These along with (A12) for mass balance at the bubble interface are the basis of the numerical model outlined by *Proussevitch et al.* [1993] and further developed here.

A3. Heat Balance and Temperature Diffusion

There are six thermal effects of bubble growth taken into account in this study (as listed in section 1). To meet the condition of energy conservation, we consider the energy equations separately for the bubble and melt. For the bubble, energy conservation demands that [*Proussevitch et al.*, 1993]

$$m_g c_P\, dT - V_g\, dP + \frac{\Delta H_{ev}}{M_w} dm_w^g + s\,\mathbf{J}\, dt = 0 \quad \text{(A16)}$$

The terms in (A16) represent enthalpy of (1) gas inside the bubble, (2) cooling due to pdV work of bubble expansion, (3) cooling due to latent heat of volatile exsolution, and (4) heating due to heat flux from the melt. In terms of enthalpy these can be written respectively as

$$dH_g + dH_{ex} + dH_{ev} + dH_{con} = 0 \quad \text{(A17)}$$

To find the first term in (A17), we can substitute gas mass from the ideal gas law if bubble pressure, radius, and gas composition are known, resulting in

$$dH_g = \frac{4\pi R^3 p_g M}{3 B T_g} c_P\, dT_g \quad \text{(A18)}$$

Enthalpy of pdV work can be written in terms of bubble radius and pressure such that

$$dH_{ex} = -\frac{4\pi}{3} R^3 dp_g \quad \text{(A19)}$$

To find the heat of gas exsolution from (A16), we need to know the change of gas mass within the bubble. In terms of mass flux through the bubble interface, (A11) and (A12) lead to

$$dH_{ev} = 4\pi R^2 D \rho \frac{\Delta H_{ev}}{M} \left(\frac{\partial x}{\partial r}\right)_{r=R} dt \quad \text{(A20)}$$

The same approach can be used to find the heat flux through the bubble interface, so that

$$dH_{con} = 4\pi R^2 \chi \rho c_m \left(\frac{\partial T}{\partial r}\right)_{r=R} dt \quad \text{(A21)}$$

Combining (A18)-(A21) we obtain an expression for the temperature of the gas in the bubble as

$$\frac{dT_g}{dt} = \frac{3 B T_g}{p_g R c_P M} \left[\rho c_m \chi \left(\frac{\partial T}{\partial r}\right)_{r=R} - \frac{\Delta H_{ev}}{M} D \rho \left(\frac{\partial x}{\partial r}\right)_{r=R} + \frac{R}{3}\frac{dp_g}{dt}\right] \quad \text{(A22)}$$

The heat balance in the melt is mainly controlled by thermal diffusion to the cooling bubble interface. Energy conservation in an incompressible fluid (Fourier-Kirchhoff equation) can be written as

$$\rho c_P \frac{DT}{Dt} = \text{div}(\kappa \text{ grad } T) + \frac{1}{2\eta}(\tau'_{ik})^2 + dQ_{vt}. \quad \text{(A23)}$$

The first term on the right of (A23) relates to thermal conductivity. The second term represents dissipative heating due to viscous resistance in the melt, and the third term is the latent heat of phase transition (crystallization or vitrification) in the liquid. The dissipative heat term in spherical coordinates is written as

$$\frac{1}{2\eta}(\tau'_{ik})^2 = 2\eta\left[\left(\frac{\partial v_r}{\partial r}\right)^2 + 2\left(\frac{v_r}{r}\right)^2\right] \quad \text{(A24)}$$

where v_r is obtained from bubble growth rate v_R of the continuity equation (A2). The last term in (A23) (heat of phase transition) merits some explanation. To avoid discontinuity, we can treat the phase transition as a process taking place in a small temperature interval so that it is applicable for eutectic or solid solution phase crystallization as well as melt vitrification [*Richet and Bottinga*, 1986]. We can write the last term in (A23) as

$$dQ_{vt} = \left(\rho H'_{vt} \frac{dT}{dt}\right)_{T<T_{vt}} \quad \text{(A25)}$$

where $H'_{vt} = \frac{\Delta H_{vt}}{\Delta T_{vt}}$ and ΔT is the interval of vitrification or eutectic crystallization [*Huppert and Sparks*, 1985].

Substituting (A24), (A2) and (A25) into (A23), we obtain

$$\frac{\partial T}{\partial t} + v_r \frac{\partial T}{\partial r} = \frac{1}{r^2}\frac{\partial}{\partial r}\left(\chi r^2 \frac{\partial T}{\partial r}\right) + 12 \frac{\nu}{c_m} v_R^2 \frac{R^4}{r^6} - \left(\frac{H'_{vt}}{c_m}\frac{dT}{dt}\right)_{T<T_{vt}} \quad \text{(A26)}$$

where $\chi = \frac{\kappa}{\rho c_P^{melt}}$ is thermal diffusivity and $\nu = \frac{\eta}{\rho}$ is kinematic viscosity. For bubble growth the boundary conditions are similar to those of the volatile diffusion equation and can be written as

$$T(r,0) = T_0 \quad r \geq R \quad t = 0 \quad \text{(A27a)}$$

$$\left(\frac{\partial T}{\partial r}\right)_{r=S} = 0 \quad t > 0 \quad \text{(A27b)}$$

$$T(R,t) = T_g \quad r = R \quad t > 0 \quad \text{(A27c)}$$

where (A27a) reflects the uniform initial temperature in the melt, (A27b) specifies no thermal exchange through the elementary cell boundary, and (A27c) sets the bubble interior to interface temperature. Equations (A26) and (A27) describe energy conservation in the melt and with (A22) for bubble temperature are used in the numerical formulation.

A4. Viscosity

Viscosity is variable in both time and space and is a function of local temperature and melt composition (volatile content). It can vary by several orders of magnitude across the bubble wall. We use the Arrhenius relation for a Newtonian liquid

$$\eta = \eta' \exp\left(\frac{E_\eta}{B T}\right) \quad \text{(A28)}$$

where $\eta' = 10^{2.5}$ Pa s [*Persikov*, 1991]. Activation energy for viscous deformation E_η is linearly dependent on composition for the composition range considered in our model [*Persikov et al.*, 1990]. It can thus be written as

$$E_\eta = E_\eta^{dry}\left(1 - k_\eta x_{volatile}\right) \quad \text{(A29)}$$

where E_η^{dry} is the activation energy for dry melt and k_η is an empirical coefficient which reflects the viscosity dependence on volatile concentration. Consequently, viscosity can be expressed as

$$\eta = \eta' \exp\left(\frac{E_\eta^{dry}\left(1 - k_\eta x_{volatile}\right)}{B T}\right) \quad \text{(A30)}$$

E_η^{dry} and k_η can be determined on the basis of at least two measurements of viscosity for different dissolved volatile concentrations. Equation (A30) is a general relation which can be used for a range of magmatic compositions (basalt-rhyolite). However, direct measurements have been made for rhyolitic systems, and an empirical relation for these systems has been suggested [*Hess and Dingwell*, 1996]

which fits the observations more precisely than the general relation in (A30).

A5. Diffusion

The equations for mass balance and diffusion (A12)-(A14) require the diffusion coefficient for total water in magmatic melts. Experimental results for water diffusivity [*Chekhmir and Epel'baum*, 1991; *Jambon et al.*, 1992; *Zhang et al.*, 1991; *Zhang and Stolper*, 1991] report molecular water diffusivity measured from quenched glasses using infrared spectroscopy [*Newman et al.*, 1986]. These studies did not evaluate total water diffusivity, but they demonstrated how it could be derived from molecular water diffusivity. On this basis the relation between total (water) and molecular (H_2O) water diffusivities is

$$D_{\text{water}} = D_{H_2O} \frac{d[H_2O]}{d[\text{water}]} \tag{A31}$$

Concentrations of molecular and total water can be found by simultaneous solution of the following:

$$\left\{ \begin{array}{l} [\text{water}] = [H_2O] + 0.5\,[OH] \\ \\ \dfrac{[OH]^2}{[H_2O]\,(1 - [H_2O] - [OH])} = K \end{array} \right\} \tag{A32}$$

The water dissociation constant K is an empirically determined constant which depends on temperature, total water concentration, etc. We have reconstructed total water diffusivity in rhyolitic melt at low water content using a dissociation constant derived from recent measurements (Y. Zhang, personal communication, 1997). Diffusivity also depends on concentration. On the basis of the fact that molecular D_{H2O} varies with concentration less than a factor of 2 in the range of 0.2 - 1.7 wt% [*Zhang et al.*, 1991], we assigned a linear relationship in which diffusivity doubles between 0.2 and 3.0 wt%. This is the only linear approximation of molecular water diffusivity which leads to a logarithmic relation of total water diffusivity as obtained by regression analysis ($r = 0.9999$). The resulting regression functions are

$$\ln D_{\text{water}} = \ln x - b - \frac{E_D}{B\,T} \tag{A33}$$

where E_D can be viewed as activation energy for diffusion. $E_D = 87300$ J mole^{-1} for rhyolite and 15200 J mole^{-1} for basalt [*Zhang et al.*, 1991; *Zhang and Stolper*, 1991]. The free coefficient b is found to be 12.574 for rhyolite and 12.49 for basalt.

A6. Heat of Vaporization

Heat of vaporization depends on pressure and temperature [*Sahagian and Proussevitch*, 1996]. The temperature dependence of heat of vaporization at low pressures can be written as

$$\frac{d\Delta H_{ev}}{dT} = \Delta c_P - 4\,B\,T\,\frac{d\left(\ln X_{H2O}^{\text{mole}}\right)}{dT} \tag{A34}$$

where X is the equilibrium molar concentration of water in the melt, which is, in turn, a function of pressure and temperature as prescribed by the solubility law. The pressure dependence at low pressures can be written as

$$\frac{d\Delta H_{ev}}{dP} = \Delta c_P \frac{T\,\tilde{V}_g}{\Delta H_{ev}} + \tilde{V}_g \left(2 + \frac{T\,\Delta c_P}{\Delta H_{ev}}\right)\left(\frac{\partial(\ln k_w)}{\partial(\ln P)}\right)_T \tag{A35}$$

where $\tilde{V}_g$ is the gas volume per mole and k_w is the Henry's analog constant [*Burnham*, 1994].

The heat of vaporization as a function of pressure and temperature is evaluated for water in the form of an empirical interpolation polynomial

$$\Delta H_{ev} = \sum_{i=0}^{5}\left[(\ln P)^i \sum_{j=0}^{2} k_{j,i}\,T^i\right] \tag{A36}$$

where the coefficients $k_{j,i}$ are listed in Table A2, ΔH_{ev} is in J mole^{-1}, P is in megapascals, and T is in kelvins. In evaluating this relation we have found that both pressure and temperature have important impacts on the heat of vaporization at low pressures, but at high pressures (>100 MPa) temperature is less important.

A7. Analytical System of Equations

The results of the previous sections define a complete system of equations which govern bubble growth in our analytical formulation. These include (A9), (A12), (A14), (A15), (A22), (A26), (A27), (A30), (A33), (A35) and (A36). For convenience they are listed together in Table 1.

Appendix B: Numerical Formulation

B1. Lagrangian Coordinate Transformation

In order to eliminate the advective terms which arise from motions of material particles in response to bubble expansion [*Anderson et al.*, 1984] we apply a Lagrangian coordinate transformation to all equations to take advantage of the spherical domain symmetry. The coordinate transformation is based on the introduction of new variables for position in terms of potential functions Φ and W, where

$$y = r^3 - R^3(t) \tag{B1}$$

$$x - x_0 = x' = \frac{\Phi}{\partial y} \tag{B2a}$$

$$T - T_0 = T' = \frac{\partial W}{\partial y} \tag{B2b}$$

These transformations will enable us to reduce both chemical and temperature diffusion equations to second-order differential equations. An additional advantage of

Table A2. Coefficients for Equation (A36)

Index	i = 0	i = 1	i = 2	i = 3	i = 4	i = 5
j = 0	6.736E+4	2.470E+3	-2.349E+3	-1.131E+3	2.591E+2	-1.089E+1
j = 1	-7.185E+1	-3.534E+0	3.650E+0	1.639E+0	-4.865E-1	2.939E-2
j = 2	2.365E-2	1.744E-3	-1.594E-3	-6.038E-4	1.984E-4	-1.270E-5

Read 6.736E+4 as 6.736×10^4.

the potential functions is the elimination of mathematical difficulties introduced when there are high initial gradients of concentration and temperature at the bubble interface.

Thus we can write equations for combined momentum and continuity

$$p_g = p_f + \frac{2\sigma}{R} - 4\nu_R R^2 \int_0^{S^3-R^3} \frac{\eta(y)}{(y+R^3)^2}\,dy \qquad \text{(B3)}$$

mass balance at the bubble interface (diffusive bubble growth)

$$d\left(\frac{P_g R^3}{T_g}\right) = 9\frac{B}{M} R^4 D\rho \left(\frac{\partial^2\Phi}{\partial y^2}\right)_{y=0} dt \qquad \text{(B4)}$$

and volatile diffusion in the melt

$$\frac{\partial\Phi}{\partial t} = 9D(y+R^3)^{4/3}\frac{\partial^2\Phi}{\partial y^2} \qquad \text{(B5)}$$

with boundary and initial conditions

$$\Phi(y,0) = 0 \quad t = 0 \qquad \text{(B6a)}$$

$$\left(\frac{\partial^2\Phi}{\partial y^2}\right)_{y=S^3-R^3} = 0 \quad t > 0 \qquad \text{(B6b)}$$

$$\left(\frac{\partial\Phi}{\partial y}\right)_{y=0} = (K_h p_g)^{1/2} - x_0 \quad t > 0 \qquad \text{(B6c)}$$

In addition, heat balance at the bubble interface and inside the bubble can be written as

$$\frac{dT_g}{dt} = \frac{9BT_g R}{p_g c_P M}\left[\rho c_m \chi\left(\frac{\partial^2 W}{\partial y^2}\right)_{y=0} - \frac{\Delta H_{ev}}{M} D\rho\left(\frac{\partial^2\Phi}{\partial y^2}\right)_{y=0} + \frac{1}{9R}\frac{dp_g}{dt}\right] \qquad \text{(B7)}$$

and temperature diffusion with internal heat generation takes the form of

$$\frac{\partial W}{\partial t} = 9\chi(y+R^3)^{4/3}\frac{\partial^2 W}{\partial y^2} - 12\frac{\nu_R^2 R^4}{\rho c_m}\int_0^{S^3-R^3}\frac{\eta(y)\,dy}{(y+R^3)^2} - \left(\frac{H'_{vt}}{c_m}\frac{dW}{dt}\right)_{T<T_{vt}} \qquad \text{(B8)}$$

with boundary and initial conditions

$$W(y,0) = 0 \quad t = 0 \qquad \text{(B9a)}$$

$$\left(\frac{\partial^2 W}{\partial y^2}\right)_{y=S^3-R^3} = 0 \quad t > 0 \qquad \text{(B9b)}$$

$$\left(\frac{\partial W}{\partial y}\right)_{y=0} = T_g - T_0 \quad t > 0 \qquad \text{(B9c)}$$

B2. Nondimensionalization and Introduction of Parameters

Nondimensionalization of the formulation through introduction of dimensionless parameters makes it possible to characterize the essential properties and processes in the system with a minimum of variables, thus facilitating numerical solution. Circumflex (^) indicates dimensionless quantities defined as

$$\hat{\Phi} = \frac{\Phi}{S_0^3 - R_0^3} = \frac{\Phi}{S^3 - R^3} \qquad \text{(B10a)}$$

$$\hat{W} = \frac{W}{T_0(S_0^3 - R_0^3)} = \frac{W}{T_0(S^3 - R^3)} \qquad \text{(B10b)}$$

$$\hat{p} = \frac{p}{p_f} \qquad \text{(B10c)}$$

$$\hat{T} = \frac{T}{T_0} \qquad \text{(B10d)}$$

$$\hat{t} = t\frac{D_0}{R_0^2} \qquad \text{(B10e)}$$

$$\hat{y} = \frac{y}{S_0^3 - R_0^3} = \frac{y}{S^3 - R^3} \qquad \text{(B10f)}$$

$$\hat{R} = \frac{R}{R_0} \qquad \text{(B10g)}$$

$$\hat{D} = \frac{D}{D_0} \qquad \text{(B10h)}$$

$$\hat{\eta} = \frac{\eta}{\eta_0} \qquad \text{(B10i)}$$

$$\Delta\hat{H} = \frac{\Delta H_{ev}}{\Delta H_{ev}^0} \qquad \text{(B10j)}$$

Concentration is not included above because it was defined as a dimensionless parameter in the formulation a priori. The potential functions and other parameters are normalized by model initial conditions and bubble dimensions. Pressure is normalized with final ambient pressure, while temperature, diffusion, viscosity, and heat of vaporization are normalized with their initial values. Thermal diffusivity, heat capacities of the melt and gas, melt density, and Henry's constant are taken as constants in the numerical formulation of bubble growth dynamics.

The analytical system of equations (Table 1) can be rewritten with dimensionless parameters from (B10a) to (B10j) to yield 10 dimensionless equation parameters (equation (B11a) - (B11j)). The first five are the same as in the case of isothermal bubble growth [*Proussevitch et al.*, 1993].

$$Y_1 = \frac{R_0^3}{S_0^3 - R_0^3} = \frac{\text{Gas volume at t=0}}{\text{Melt volume}} \tag{B11a}$$

$$Y_2 = \frac{\rho\, B\, T_0}{M\, p_f} = \frac{\rho_{melt}}{\rho_{gas}} \tag{B11b}$$

$$Y_3 = \frac{2\,\sigma}{R_0\, p_f} = \frac{p_{\sigma,0}}{p_f} \tag{B11c}$$

$$Y_4 = \frac{4\,\eta_0\, D_0}{p_f\, R_0^2} = \frac{p_\tau}{p_f} \tag{B11d}$$

$$Y_5 = \left(K_h\, p_f\right)^{1/2} = x_{w,f} \tag{B11e}$$

$$Y_6 = \mathrm{Le} = \frac{\chi}{D_0} \tag{B11f}$$

$$Y_7 = \frac{12\,\eta_0\, D_0}{R_0^2\,\rho\, c_m\, T_0} = \frac{H_\tau}{H_m} \tag{B11g}$$

$$Y_8 = \frac{c_m}{c_P} = \frac{c_m^{melt}}{c_P^{gas}} \tag{B11h}$$

$$Y_9 = \frac{\Delta H_0}{M\, c_m\, T_0} = \frac{\Delta H_{ev}}{H_m} \tag{B11i}$$

$$Y_{10} = \frac{H'_{vt}}{c_m} \tag{B11j}$$

Y_1 reflects the initial volumetric gas fraction in the system; Y_2 is the gas-melt density ratio at ambient pressure; Y_3 and Y_4 represent the surface tension and stress tensor ratios with final ambient pressure, respectively; Y_5 is water (volatile) concentration at p_f; Y_6 is the Lewis number; Y_7 reflects viscous dissipative heating of the melt; Y_9 represents cooling due to the heat of vaporization; Y_8 is the ratio of melt and gas heat capacities; and Y_{10} is the ratio of heating of the melt due to temperature-normalized vitrification (or crystallization) melt to heat capacity.

Substitution of the dimensionless variables in (B10) and parameters in (B11) results in the dimensionless form of the governing system of equations (B12), given here in the same sequence as in Table 1.

$$\hat{p}_g = 1 + \frac{Y_3}{\hat{R}} + Y_1\, Y_4\, \hat{R}^2\, \hat{v}_{\hat{R}} \int_0^1 \frac{\hat{\eta}\, d\hat{y}}{\left(\hat{y} + Y_1\, \hat{R}^3\right)^2} \tag{B12a}$$

$$\frac{d}{d\hat{t}}\left(\frac{\hat{p}_g\, \hat{R}^3}{\hat{T}_g}\right) = 9\, Y_1\, Y_2\, \hat{R}^4 \left(\frac{\partial^2 \hat{\Phi}}{\partial \hat{y}^2}\right)_{\hat{y}=0} \tag{B12b}$$

$$\frac{\hat{\Phi}}{\partial \hat{t}} = 9\, Y_1^{2/3} \left(\hat{y} + Y_1\, \hat{R}^3\right)^{4/3} \frac{\partial^2 \hat{\Phi}}{\partial \hat{y}^2} \tag{B12c}$$

$$\hat{\Phi}(\hat{y},0) = 0 \quad \hat{t} = 0 \tag{B12d}$$

$$\left(\frac{\hat{\Phi}}{\partial \hat{y}}\right)_{\hat{y}=0} = Y_5\, \hat{p}_g^{1/2} - \hat{x}_0 \quad \hat{t} > 0 \tag{B12e}$$

$$\left(\frac{\partial^2 \hat{\Phi}}{\partial \hat{y}^2}\right)_{\hat{y}=1} = 0 \quad \hat{t} > 0 \tag{B12f}$$

$$\frac{d\hat{T}_g}{d\hat{t}} = 9\, Y_1\, Y_2\, Y_8\, \frac{\hat{T}_g\, \hat{R}}{\hat{p}_g} \left[\mathrm{Le}\left(\frac{\partial^2 \hat{W}}{\partial \hat{y}^2}\right)_{\hat{y}=0} - Y_9\, \Delta\hat{H}\, \hat{D}\left(\frac{\partial^2 \hat{\Phi}}{\partial \hat{y}^2}\right)_{\hat{y}=0} + \frac{Y_7}{27\, Y_1\, Y_4\, \hat{R}}\, \frac{d\hat{p}_g}{d\hat{t}}\right] \tag{B12g}$$

$$\left(1 + Y_{10}\right)_{T<T_{vt}} \frac{\partial \hat{W}}{\partial \hat{t}} = 9\, \mathrm{Le}\, Y_1^{2/3} \left(\hat{y} + Y_1\, \hat{R}^3\right)^{4/3} \frac{\partial^2 \hat{W}}{\partial \hat{y}^2} - Y_1^2\, Y_7\, \hat{v}_{\hat{R}}^2\, \hat{R}^4 \int_0^1 \frac{\hat{\eta}(\hat{y})\, d\hat{y}}{\left(\hat{y} + Y_1\, \hat{R}^3\right)^2} \tag{B12h}$$

$$\hat{W}(\hat{y},0) = 0 \quad \hat{t} = 0 \tag{B12i}$$

$$\left(\frac{\partial \hat{W}}{\partial \hat{y}}\right)_{\hat{y}=0} = \hat{T}_g - 1 \quad \hat{t} > 0 \tag{B12j}$$

$$\left(\frac{\partial^2 \hat{W}}{\partial \hat{y}^2}\right)_{\hat{y}=1} = 0 \quad \hat{t} > 0 \tag{B12k}$$

$$\hat{\eta}(\hat{y}) = f\left(T(\hat{y}), x(\hat{y})\right) \tag{B12l}$$

see also (A30) and (B10i)

$$\hat{D}(\hat{y}) = f\left(T(\hat{y}), x(\hat{y})\right) \tag{B12m}$$

see also (A33)

$$\widehat{\Delta H} = f(T_g, p_g) \qquad \text{(B12n)}$$

see also (A35), (A36), and (B10j).

Acknowledgments. The authors are grateful to A.T. Anderson for very helpful discussions of the model application and selecting melt properties. Thanks also to Y. Zhang for discussions regarding water diffusion and dissipative energy and a review of the physical and mathematical formulation as well as access to unpublished data. The authors appreciate insightful reviews by F. Dobran, F. Spera, A. Toramaru, and B. Wanamaker. This research was supported by NSF grant EAR-9496287.

References

Alidibirov, M.A., A model for viscous magma fragmentation during volcanic blasts, *Bull. Volcanol., 56*, 459-465, 1994.

Ammar, M.M., S.A. Gharib, M.M. Halawa, H.A. El-Batal, and K. El-Badry, Thermal conductivity of silicate and borate glasses, *J. Am. Ceram. Soc., 66*, 76-77, 1983.

Anderson, A.T.J., Hourglass inclusions: Theory and application to the Bishop Rhyolitic Tuff, *Am. Mineral., 76*, 530-547, 1991.

Anderson, A.T.J., C.M. Skirius, F. Lu, and A.M. Davis, Preeruption gas content of Bishop Plinian rhyolitic magma, *Geol. Soc. Am. Abstr. Programs, 21*, 270, 1989.

Anderson, D.A., J.C. Tannehill, and R.H. Pletcher, *Computational Fluid Mechanics and Heat Transfer*, 599 pp., Hemisphere, Washington, D.C., 1984.

Arefmanesh, A., S.G. Advani, and E.E. Michaelides, An accurate numerical solution for mass diffusion-induced bubble growth in viscous liquids containing limited dissolved gas, *Int. J. Heat Mass Transfer, 35*, 1711-1722, 1992.

Bacon, C.R., High-temperature heat content and heat capacity of silicate glasses: Experimental determination and a model for calculation, *Am. J. Sci., 277*, 109-135, 1977.

Bagdassarov, N.S., and D.B. Dingwell, A rheological investigation of vesicular rhyolite, *J. Volcanol. Geotherm. Res., 50*, 307-322, 1992.

Bagdassarov, N.S., and D.B. Dingwell, Deformation of foamed rhyolites under internal and external stresses: An experimental investigation, *Bull. Volcanol., 55*, 147-154, 1993.

Bagdassarov, N.S., D.B. Dingwell, and S.L. Webb, Viscoelasticity of crystal-bearing and bubble-bearing rhyolite melts, *Phys. Earth Planet. Inter., 83*, 83-99, 1994.

Bottinga, Y., and M. Javoy, MORB degassing: Bubble growth and ascent, *Chem. Geol., 81*, 225-270, 1990.

Burnham, C.W., Water in magmas: A mixing model, *Geochim. Cosmochim. Acta, 39*, 1077-1084, 1975.

Burnham, C.W., Development of the Burnham model for prediction of H_2O solubility in magmas, in *Volatiles in Magmas*, edited by M.R. Carroll and J.R. Holloway, pp. 123-129, Mineral. Soc. of Am., Washington, D.C., 1994.

Carey, S., and H. Sigurdsson, Temporal variations in column height and magma discharge rate during the 79 A.D. eruption of Vesuvius, *Geol. Soc. Am. Bull., 99*, 303-314, 1987.

Carey, S.N., H. Sigurdsson, and J.E. Gardner, Variations of column height and magma discharge during the May 18, 1980, eruption of Mount St. Helens, *J. Volcanol. Geotherm. Res., 43*, 99-112, 1990.

Carrigan, C., and A. McBirney, Experimental determination of the thermal conductivity of molten $CaMgSi_2O_6$ and the transport of heat through magmas: Comment, *J. Geophys. Res., 102*, 15,073-15,076, 1997.

Cashman, K.V., and M.T. Mangan, Physical aspects of magma degassing, II, Constraints on vesiculation processes from textural studies of eruptive products, in *Volatiles in Magmas*, edited by M.R. Carroll, and J.R. Holloway, pp. 446-478, Mineral. Soc. of Am., Washington, D. C., 1994.

Chekhmir, A.S., and M.B. Epel'baum, Diffusion in magmatic melts: New study, in *Physical chemistry of magmas*, edited by L.L. Perchuk and I. Kushiro, pp. 99-119, Springer-Verlag, New York, 1991.

Clark, S., F.J. Spera, and D.A. Yuen, Steady state double-diffusive convection in magma chambers heated from below, in *Magmatic Processes: Physiochemical Principles*, edited by B.O. Mysen, pp. 289-305, Geochem. Soc., Washington, D. C., 1987.

Dobran, F., Nonequilibrium flow in volcanic conduits and applications to the eruptions of Mount St. Helens on May 18, 1980, and Vesuvius in A.D. 79, *J. Volcanol. Geotherm. Res., 49*, 285-311, 1992.

Dobran, F., and S. Coniglio, Magma ascent simulations of Etna's eruptions aimed at internal system definition, *J. Geophys. Res., 101*, 713-731, 1996.

Dunbar, C., and P. Kyle, Volatile contents of obsidian clasts in tephra from the Taupo volcanic zone, New Zealand: Implications to eruptive processes, *J. Volcanol. Geotherm. Res., 49*, 127-145, 1992.

Eichelberger, J.C., and H.R. Westrich, Magmatic volatiles in explosive rhyolitic eruptions, *Geophys. Res. Lett., 8*, 757-760, 1981.

Epstein, P.S., and M.S. Plesset, On the stability of gas bubbles in liquid-gas solutions, *J. Chem. Phys., 18*, 1505-1509, 1950.

Gardner, J.E., H. Sigurdsson, and S.N. Carey, Eruption dynamics and magma withdrawal during the plinian phase of the Bishop Tuff eruption, Long Valley Caldera, *J. Geophys. Res., 96*, 8097-8111, 1991.

Harris, D.M., Ascent and crystallization of albite and granitic melts saturated with H_2O, *J. Geology, 85*, 451-459, 1977.

Hess, K.U., and D.B. Dingwell, Viscosities of hydrous heucogranitic melts: A non-Arrhenian model, *Am. Mineral., 81*, 1297-1300, 1996.

Huppert, H.E., and R.S.J. Sparks, Cooling and contamination of mafic and ultramafic magmas during ascent through continental crust, *Earth Planet. Sci. Lett., 74*, 371-386, 1985.

Jambon, A., Y. Zhang, and E.M. Stolper, Experimental dehydration of natural obsidian and estimation of D_{H2O} at low water contents, *Geochim. Cosmochim. Acta, 56*, 2931-2935, 1992.

Johnson, M.C., A.T. Anderson, and M.J. Rutherford, Pre-eruptive volatile contents in magmas, in *Volatiles in Magmas*, edited by M.R. Carroll and J.R. Holloway, pp. 281-330, Mineral. Soc. of Am., Washington, D.C., 1994.

Landau, L.D., and E.M. Lifshitz, *Fluid Mechanics*, 539 pp., Pergamon, Tarytown, N. Y., 1987.

Melson, W.G., J.F. Allan, D.R. Jerez, J. Nelen, M.L. Calvache, S.N. Williams, J. Fournelle, and M. Perfit, Water contents, temperatures and diversity of the magmas of the catastrophic eruption of Nevado-Del-Ruiz, Columbia, November 13, 1985, *J. Volcanol. Geotherm. Res., 41*, 97-126, 1990.

Murase, T., and A. McBirney, Properties of some common igneous rocks and their melts at high temperature, *Geol. Soc. Am. Bull., 83*, 3563-3592, 1973.

Mysen, B., The solubility of H_2O and CO_2 under predicted magma genesis conditions and some petrological and geophysical implications, *Rev. Geophys., 15*, 251-261, 1977.

Neal, C., T. Duggan, E. Wolfe, and E. Brandt, Lava samples, temperatures and compositions, in *The Puu Oo Eruption of Kilauea Volcano, Hawaii Episodes 1-20, Jan. 3, 1983 Through June 8, 1984*, edited by E.W. Wolfe, pp. 99-126, U.S. Geol. Surv., Denver, Colo., 1988.

Neri, A., and F. Dobran, Influence of eruption parameters on the thermofluid dynamics of collapsing volcanic columns, *J. Geophys. Res.*, *99*, 11,833-11,857, 1994.

Neuville, D.R., P. Courtial, D.B. Dingwell, and P. Richet, Thermodynamic and rheological properties of rhyolite and andesite melts, *Contrib. Mineral. Petrol.*, *113*, 572-581, 1993.

Newman, S., E. Stolper, and S. Epstein, Measurement of water in rhyolitic glasses: Calibration of an infrared spectroscopic technique, *Am. Mineral.*, *71*, 1527-1541, 1986.

Perry, R.H., D.W. Green, and J.O. Maloney, *Perry's Chemical Engineers' Handbook*, McGraw-Hill, New York, 1984.

Persikov, E.S., The viscosity of magmatic liquids: Experiment, generalized patterns, a model for calculation and prediction, applications., in *Physical Chemistry of Magmas*, edited by L.L. Perchuk and I. Kushiro, pp. 1-40, Springer-Verlag, New York, 1991.

Persikov, E.S., V.A. Zharikov, P.G. Bukhtiyarov, and S.F. Pol'skoy, The effect of volatiles on the properties of magmatic melts, *Eur. J. Mineral.*, *2*, 621-642, 1990.

Princen, H., Highly concentrated emulsions, I, *J. Colloid Interface Sci.*, *71*, 55-66, 1979.

Proussevitch, A., and V. Kutolin, Surface tension of magmatic melts (in Russian), *Geol. Geophys.*, *9*, 58-67, 1986.

Proussevitch, A.A., and D.L. Sahagian, Dynamics of coupled diffusive and decompressive bubble growth in magmatic systems, *J. Geophys. Res.*, *101*, 17,447-17,455, 1996.

Proussevitch, A.A., D.L. Sahagian, and A.T. Anderson, Dynamics of diffusive bubble growth in magmas: Isothermal case, *J. Geophys. Res.*, *98*, 22,283-22,308, 1993.

Richet, P., and Y. Bottinga, Glass transition and thermodynamic properties of $NaAlSi_nO_{2n-z}$ and $KAlSi_3O_8$, *Geochim. Cosmochim. Acta*, *48*, 453-470, 1984.

Richet, P., and Y. Bottinga, Thermomechanical properties of silicate glasses and liquids: A review, *Rev. Geophys.*, *24*, 1-25, 1986.

Rosner, D.E., and M. Epstein, Effects of interface kinetics, capillarity and solute diffusion on bubble growth rates in highly supersaturated liquids, *Chem. Eng. Sci.*, *27*, 69-88, 1972.

Sahagian, D.L., and A.T. Anderson, Classification of Hawaiian eruption styles on the basis of mechanisms of volatile release (abstract), *Eos Trans. AGU*, *72*, 296, 1991.

Sahagian, D.L., and A.A. Proussevitch, Thermal effects of magma degassing, *J. Volcanol. Geotherm. Res.*, *74*, 19-38, 1996.

Sahagian, D.L., A.A. Proussevitch, and A.T. Anderson, Reply, *J. Geophys. Res.*, *99*, 17,829-17,832, 1994.

Scriven, L.E., On the dynamic of phase growth, *Chem. Eng. Sci.*, *10*, 1-13, 1959.

Shaw, H.R., T.L. Wright, K.L. Peck, and R. Okamura, The viscosity of basaltic magma: An analysis of field measurements in Makaopuhi Lava Lake, Hawaii, *Am. J. Sci.*, *266*, 225-264, 1968.

Silver, L.A., P.D. Ihinger, and E. Stolper, The influence of bulk composition on the speciation of water in silicate glasses, *Contrib. Min.eral Pet.rol*, *104*, 142-162, 1990.

Snyder, D., E. Gier, and I. Carmichael, Experimental determination of the thermal conductivity of molten $CaMgSi_2O_6$ and the transport of heat through magmas, *J. Geophys. Res.*, *99*, 15,503-15,516, 1994.

Snyder, D., E. Gier, and I. Carmichael, Experimental determination of the thermal conductivity of molten $CaMgSi_2O_6$ and the transport of heat through magmas: Reply, *J. Geophys. Res.*, *102*, 15077-15080, 1997.

Sparks, R.S.J., The dynamics of bubble formation and growth in magmas: A Review and analysis, *J. Volcanol. Geotherm .Res.*, *3*, 1-38, 1978.

Sparks, R.S.J., Comment on "Dynamics of diffusive bubble growth in magmas: Isothermal case" by A. A. Proussevitch, D. L. Sahagian, and A. T. Anderson, *J. Geophys. Res.*, *99*, 17,827-17,828, 1994.

Sparks, R.S.J., J. Barclay, C. Jaupart, H.M. Mader, and J.C. Phillips, Physical aspects of magma degassing, 1, Experimental and theoretical constraints on vesiculation, in *Volatiles in Magmas*, edited by M.R. Carroll and J.R. Holloway, pp. 413-445, Mineral. Soc. of Am., Washington, D. C., 1994.

Stebbins, J.F., I.S.E. Carmichael, and L.K. Moret, Heat capacities and entropies of silicate liquids and glasses, *Contrib. Mineral. Petrol.*, *86*, 131-148, 1984.

Stolper, E., and J. Holloway, Experimental determination of the solubility of carbon dioxide in molten basalt at low pressure, *Earth Planet. Sci. Lett.*, *87*, 397-408, 1988.

Szekely, J., and S. Fang, Non-equilibrium effects in the growth of spherical gas bubbles due to solute diffusion, II, *Chem. Eng. Sci.*, *28*, 2127-2140, 1973.

Toramaru, A., Vesiculation process and bubble size distributions in ascending magmas with constant velocities, *J. Geophys. Res.*, *94*, 17,523-17,542, 1989.

Toramaru, A., Numerical study of nucleation and growth of bubbles in viscous magmas, *J. Geophys. Res.*, *100*, 1913-1931, 1995.

Verhoogen, J., Mechanics of ash formation, *Am. J. Sci.*, *249*, 729-739, 1951.

Weast, R.C., *Handbook of Chemistry and Physics*, CRC Press, Boca Raton, Fla,, 1976.

Webb, S.L., and D.B. Dingwell, Non-Newtonian rheology of igneous melts at high stresses and strain rates: Experimental results for rhyolite, andesite, basalt, and nephelinite, *J. Geophys. Res.*, *95*, 15,695-15,702, 1990.

Westrich, H., H. Stockman, and J. Eichelberger, Degassing of rhyolitic magma during ascent and emplacement, *J. Geophys. Res.*, *93*, 6503-6511, 1988.

Wilson, L., Relationships between pressure, volatile content and ejecta velocity in three types of volcanic eruptions, *J. Volcanol. Geotherm. Res.*, *8*, 297-314, 1980.

Wilson, L., R.S.J. Sparks, and G.P.L. Walker, Explosive volcanic eruptions, IV, The control of magma properties and conduit geometry on eruption column behaviour, *Geophys. J. R. Astron. Soc.*, *63*, 117-148, 1980.

Wohletz, K.H., M.F. Sheridan, and W.K. Brown, Particle size distributions and the sequential fragmentation transport theory applied to volcanic ash, *J. Geophys. Res.*, *94*, 15,703-15,721, 1989.

Zhang, Y., and E.M. Stolper, Water diffusion in a basaltic melt, *Nature*, *351*, 306-309, 1991.

Zhang, Y., E. Stolper, and G. Wasserburg, Diffusion of water in rhyolitic glasses, *Geochim. Cosmochim. Acta*, *55*, 441-456, 1991.

Zhang, Y., E.M. Stolper, and P. Ihinger, Kinetics of the reaction $H_2O+O<->2OH$ in rhyolitic and albitic glasses: Preliminary results, *Am. Mineral.*, *80*, 593-612, 1995.

A. A. Proussevitch and D. L. Sahagian, Institute for the Study of Earth, Oceans, and Space, University of New Hampshire, Durham, NH 03824-3525. (e-mail: alex.proussevitch@unh.edu; dork.sahagian@unh.edu.)

(Received May 30, 1987; revised March 4, 1998; accepted March 11, 1998.)